Diffuse degassing at Longonot Volcano, Kenya: implications for CO_2 flux in continental rifts.

Elspeth Robertson[1]; Juliet Biggs[1]; Marie Edmonds[2]; Laura Clor[3,4]; Tobias P. Fischer[3]; Charlotte Vye-Brown[5]; Gladys Kianji[6]; Wesley Koros [7,8], Risper Kandie[8].

[1]COMET, School of Earth Sciences, University of Bristol.

[2] COMET, Department of Earth Sciences, University of Cambridge.

[3] Department of Earth and Planetary Sciences, University of New Mexico.

[4] USGS, Menlo Park, California.

[5] British Geological Survey

[6] Department of Geology, University of Nairobi.

[7] Department of Engineering Science, University of Auckland

[8] Kenya Electricity Generating Company Ltd. (KenGen), Naivasha, Kenya

Corresponding Author: Juliet Biggs. juliet.biggs@bristol.ac.uk; School of Earth Sciences, Wills Memorial Building, University of Bristol, Queens Road, Bristol, BS8 1RJ.

Highlights:

- CO_2 flux at Longonot volcano, Kenya is <300 kg d^{-1} mostly along crater faults
- Carbon isotope values indicate dominantly magmatic source.
- Gas flux is low despite historical eruption (1863), recent unrest (2004-6).
- Lower flux than nearby faulted basins, with implications for magma storage regimes.

Abstract

Magma movement, fault structures and hydrothermal systems influence volatile emissions at rift volcanoes. Longonot is a Quaternary caldera volcano located in the southern Kenyan Rift, where regional extension controls recent shallow magma ascent. Here we report the results of a soil carbon dioxide (CO_2) survey in the vicinity of Longonot Volcano, as well as fumarolic gas compositions and carbon isotope data. The total non-biogenic CO_2 degassing is estimated at <300 kg d^{-1}, and is largely controlled by crater faults and fractures close to the summit. Thus, recent volcanic structures, rather than regional tectonics, control fluid pathways and degassing. Fumarolic gases are characterised by a narrow range in carbon isotope ratios ($\delta^{13}C$), from -4.7 ‰ to -6.4 ‰ (vs. PDB) suggesting a magmatic origin with minor contributions from biogenic CO_2. Comparison with other degassing measurements in the East African Rift show that records of historical eruptions or unrest do not correspond directly to the magnitude of CO_2 flux from volcanic centres, which may instead reflect the current size and characteristics of the subsurface magma reservoir. Interestingly, the integrated CO_2 flux from faulted rift basins is reported to be an order of magnitude higher than that from any of the volcanic centres for which CO_2 surveys have so far been reported.

1. Introduction

Over a hundred volcanoes exist in the East African Rift and Red Sea Region (EARR), of which more than half show signs of unrest or activity (Figure 1A; Brown et al., 2015; Fournier et al., 2010a). There is abundant evidence that the silicate and carbonatite magmas of the EARR are rich in volatiles, including carbon dioxide (CO_2), sulfur, water and halogens (Darling et al., 1995; de Moor et al., 2013; Fischer et al., 2009a; Hudgins et al., 2015; Koepenick et al., 1996; Macdonald and Scaillet, 2006). In addition, primary carbonates have been found in peralkaline lavas at Suswa, Kenya (Macdonald et al., 1993), at Ol Doinyo Lengai, Tanzania (Dawson et al., 1994) and at many other volcanic centers in the region (Deans and Roberts, 1984; Ridolfi et al., 2006; Rudnick and McDonough, 1993).

Over the past 15 years, at least 15 EARR volcanoes have erupted and ground displacement has been observed at many more volcanoes. Furthermore, four crustal dyking events have been detected (Figure 1B), implying the presence of active magmatic systems beneath the rift and the prevalence of shallow magmatic intrusions (Belachew et al., 2011; Biggs et al., 2009a, 2009b, 2011a, 2013a, 2013c;

Grandin et al., 2009; Nobile et al., 2012; Pallister et al., 2010; Wright et al., 2006). The region is further characterised by extensive and mature geothermal systems and heat advected by magmatic fluids that sustains hydrothermal systems, which typically form beneath long-lived axial rift volcanoes (Omenda, 1998; Riaroh and Okoth, 1994; Wamalwa and Serpa, 2013).

The EARR is therefore a significant source of outgassing mantle volatiles, yet there is only limited understanding of the gas fluxes from the EARR and how they are controlled by volcanic structures and modulated by both the tectonics of the region and the hydrothermal systems. Understanding the carbon output of continental rifts is a topic of great interest owing to the debates over whether the ingassing (via subduction) and outgassing (via volcanism) carbon budgets of the solid Earth balance. It seems likely that rift environments might have been associated with very large outputs of CO_2 over geological time and also in the present day (Hudgins et al., 2015). Lee et al (2016) investigated diffuse degassing from a section in the Eastern Branch of EARR and show that massive and prolonged mantle CO_2 emissions are prevalent along extensional faults which act as fluid flow pathways. Gas fluxes are also of potential importance for monitoring unrest and forecasting eruptions (Sparks, 2003); for understanding geothermal systems for commercial gain (Lewicki and Oldenburg, 2004); and for mitigating risks due to CO_2 inundation or accumulation in topographic lows, which is a significant hazard to human health (Kling et al., 1987).

Active outgassing from volcanoes during eruptions occurs from vents or fissures. Diffuse degassing of magmatic or hydrothermal fluids may occur through soils, from fumaroles and from hot springs. Studies show that volcanic systems can release large quantities of CO_2 through soil degassing between and during eruptions (Allard et al., 1991; Bergfeld et al., 2001; Brombach and Hunziker, 2001; Cardellini et al., 2003; Chiodini et al., 1998; Chiodini et al., 1996; Notsu et al., 2005; Werner et al., 2000). Faults and fractures (both tectonic and volcanic) often focus the ascent of CO_2-rich fluids. At large caldera-forming volcanic centers such as Yellowstone (USA) and Campi Flegrei (Italy), fluxes reach 1.5 – 4.5 k t d^{-1} CO_2, likely sourced from deep magma reservoirs whereby the fluids migrate to the surface along tectonic structures (Chiodini et al., 2001; Granieri et al., 2010; Werner and Brantley, 2003). At Somma-Vesuvius (Italy), the ascent of mantle-sourced CO_2 is controlled by basement lineaments aligned along the regional stress field (Aiuppa et al., 2004). In contrast, degassing is controlled by local volcanic structures at Santorini (Greece) and Etna (Italy), and has been used to detect buried active faults (Barberi and Carapezza, 1994; Giammanco et al., 1997). For Etna, up to 50% of CO_2 emissions emanate diffusely through the volcanic flanks, bypassing the main volcanic vent (Giammanco et al., 1997).

Diffuse degassing of magmas in rifting environments has been little studied. However, it has long been speculated that rift volcanoes represent a significant, but unquantified, source of atmospheric CO_2 (Koepenick et al., 1996). Magma ascent and storage in these regions can be controlled by regional structures associated with extension, pre-existing basement heterogeneities and volcano- tectonic structures (Abebe et al., 2007; Nobile et al., 2012). In the Natron-Magadi region of Kenya and Tanzania, deep crustal faults are pathways for CO_2 likely derived from crustal magma bodies that are stalled and degassing at depth (Lee et al., 2016). At Aluto volcano (Ethiopia), elevated soil CO_2 fluxes occur along both major faults and volcanic structures and demonstrate the complex interaction between both structures and degassing. In addition, topography and lithological heterogeneities influence degassing sites (Hutchison et al., accepted). During quiescent periods at Ol Doinyo Lengai (Tanzania), diffuse soil CO_2 emissions account for only <2 % of the total flux (6,000 – 7,200 t d^{-1}), with the remaining emissions originating from seven crater vents (Koepenick et al., 1996).

Geothermal systems are prevalent at young rift volcanoes and CO_2 is the dominant gas constituent in hydrothermal fluids. Soil CO_2 degassing studies in Iceland have been used to constrain the minimum heat flow from a geothermal reservoir (Fridriksson, 2016), as well as volcano-hydrothermal flux rates (Dereinda, 2008). For instance, volcano-hydrothermal emissions at Hengill are calculated at <165 x 10^6 kg yr^{-1} CO_2, (Hernández et al., (2012) and diffuse geothermal emissions at Krafla reach 84 x 10^6 kg yr^{-1} CO_2 (Armannsson et al., 2005). Hydrothermal systems likely have an important role in modifying and/or controlling volatile flux from rift volcanoes. By combining gas measurements with basaltic emplacement rates and regional fluid discharge rates, the total CO_2 flux from Iceland has been estimated to be 0.2–23 × 10^{10} mol yr^{-1}, equivalent to ~0.1–10% of the estimated global ridge flux (Barry et al., 2014).

This study presents a soil CO_2 degassing survey at Longonot volcano (Kenyan Rift). Between 2004 and 2006, the volcano experienced edifice-wide ground uplift of ~9 cm, followed by slow subsidence at a rate of <0.5 cm yr^{-1} (Biggs et al., 2009b). The presence of fumaroles and an extensive hydrothermal system at Longonot suggests active input of magmatic heat and volatiles into the system (Alexander and Ussher, 2011; Dunkley et al., 1993). The origin of the deformation at Longonot is likely linked to the presence of an active magma body in the crust that is influencing the behavior of a shallow hydrothermal system (Biggs et al., 2009b; Biggs et al., 2016). Longonot therefore represents a good opportunity to understand complex and long-lived hydrothermal systems in the presence of magma bodies supplying heat and volatiles.

The aim of this paper is to identify the characteristics of CO_2 degassing at Longonot in order to assess the significance of emissions for the presence of stored magma at depth, its role in sustaining the hydrothermal system and the tectonic control of degassing in a rifting environment. We first investigate the structural control on degassing at Longonot using satellite imagery overlain on a British Geological Survey (BGS) map to identify volcanic and tectonic structures that may represent permeable pathways for fluid migration and outgassing. Using this information and results from a diffuse soil CO_2 survey, we estimate the total CO_2 output from Longonot and use these results to extrapolate diffuse emissions from that section of the EARR and comment on the implications for global volcanic CO_2 flux estimates.

2. Regional setting and magmatic activity

2.1 East African Rift

The EARR is comprised of the East African Rift, the Afar Triangle, the Gulf of Aden and Red Sea Rift. Within the EARR, there are 106 volcanoes, of which 18 are classed as active, 38 as restless and 50 as fully dormant (Siebert et al., 2010) (Figure 1A). Many active volcanoes are located in northern EARR (e.g. Ethiopia and Eritrea), although some are situated at the southernmost extent of the rift (Tanzania).

Since 1997, rift-scale InSAR surveys have detected at least 22 deforming volcanoes in the EARR, indicating the presence of active magmatic systems or perturbed hydrothermal systems (Biggs et al., 2009b; Biggs et al., 2011a; Biggs et al., 2013b; Biggs et al., 2013c; Fournier et al., 2010b; Pagli et al., 2012) (Figure 1A). Some volcanoes erupt (e.g. Ol Doinyo Lengai, Tanzania), others show pulse(s) of uplift and subsidence patterns, e.g. Longonot and Paka (Kenya), and Aluto and Haledebi (Ethiopia), whilst others display singular subsidence events, such as Menengai and Suswa (both Kenya). The latter type of event is more unusual and does not fit the traditional volcanic cycle model; consequently, the cause of deformation is more difficult to explain.

Dyke emplacement accommodates extension at some continental rift settings, and studies of East Africa reveal that large volumes of melt can be emplaced in this way (Hammond et al., 2011; Keranen et al., 2004a). Dykes may reach the surface and erupt, or more commonly, they stall at a few kilometres from the surface. Since 2004, four dyke events have been observed throughout the EARR (Figure 1B): Dallol (Ethiopia) in 2004 (Nobile et al., 2012), Dabbahu (Ethiopia) between 2005 – 2009 (Wright et al., 2006), Lake Natron (Tanzania) in 2007 (Biggs et al., 2009a; Calais et al., 2008), and Harrat Lunayyir (Saudi Arabia) in 2009 (Pallister et al., 2010). Between 2004 – 2010, ESA's Envisat satellite acquired regular background imagery of the EARR. It is therefore reasonable to assume that all dyking events that can be observed using satellite imagery have been detected.

The volcanic and magmatic activity in the EARR is ultimately the result of the dynamic processes occurring in the underlying mantle. Mantle processes are to a large extent driven by the African Superplume (Behn et al., 2004; Castillo et al., 2014; Ebinger and Sleep, 1998; Pik et al., 2006; Ritsema et al., 1998; Stamps et al., 2014) and seismic data as well as the widespread occurrence of mantle xenoliths show compelling evidence for extensive mantle metasomatism in the EARR (Baptiste et al., 2015; Chesley et al., 1999; Hui et al., 2015; Vauchez et al., 2005). Petrological work on samples from throughout the EARR show only slightly elevated mantle potential temperatures, despite the slow seismic velocities in the region, implying that CO_2 assisted melt production is prevalent throughout the rift (Rooney et al., 2012). Ol Doinyo Lengai is one of the largest global emitters of volcanic CO_2 and world's only currently active carbonatite volcano. The gases discharging from Ol Doinyo Lengai have clear upper mantle volatile abundance ratios and noble gas, C and N isotope compositions. This implies that extremely small mantle melt fractions are responsible for the generation of these CO_2 rich melts (Fischer et al., 2009b) consistent with extreme enrichment of H_2O and CO_2 in nepheline hosted melt inclusions (De Moor et al., 2013).

2.2 Longonot Volcano, Kenya

Longonot volcano is situated in the southern Kenyan Rift and is one of 12 Quaternary volcanoes that line the central rift grabens. It is a large caldera volcano, consisting of a relatively modern trachyte cone situated within a 12 km caldera structure (Figure 2). The geology and volcanic history of Longonot is described in detail in a number of studies (Clarke et al., 1990; Rogers et al., 2004b; Scott, 1980; Scott and Skilling, 1999). In summary, its history can be subdivided into three distinct stages (Rogers et al., 2004a). The first “Olongonot” stage occurred between 0.4 and c. 21,000 years BP with the formation of a large composite trachyte cone and ending with the incremental collapse of a 7.5 km caldera at c. 21,000 years BP. A second “caldera pyroclastic” phase was characterised by ignimbrites, surge deposits and pyroclastic fall deposits with pumices dated at 9150 ± 150 years BP (Clarke et al., 1990). The third stage commenced with an abrupt shift to effusive eruptive activity wherein a protracted sequence of trachyte lavas accumulated on the eastern edge of the caldera, forming the modern Longonot cone. The end of the third stage is marked by a large explosive eruption that produced an extensive ash fall deposit, the “Longonot Ash”, ^{14}C-dated at 3280 ± 120 years BP (Clarke et al., 1990). The collapse of a pit crater on the volcano summit was either concurrent with, or followed shortly after the ash fall deposit. The most recent activity was the eruption of two lava flows on the northern and southwestern flanks in 1863 ± 5. These trachyte a’a’ lava flows stand out from the surrounding deposits due to lack of vegetation. Over Longonot’s eruptive history, three rock types dominate: peralkaline trachyte lavas, mixed hawaiite-peralkaline lava flows, and peralkaline trachyte pyroclastic rocks (Clarke et al., 1990).

Scott et al (1980) produced the first geological map of Longonot, updated by Dunkley et al (1993) at 1:100,000 for a geothermal surface exploration study by the Kenyan Ministry of Energy and the British Geological Survey (BGS). Longonot’s eastern flank is situated <8 km from the NNW-trending rift border faults. Dunkley et al (1993) highlight a major NNW–SSE alignment of eruption centres and fissures at the volcano, passing through the summit crater (Figure 2A). They also identified minor volcanic alignments, including eruption centres, located on fissures that extend radially from the summit crater. The report produced the first systematic map of fumaroles at Longonot, identifying >50 within the crater, three on the southern caldera wall and fossil fumaroles on the pyroclastic cones. In the crater, fumaroles were located on talus slopes at the base of the vertical crater wall and emitted steam through fractures altering the surrounding rock to red iron-oxides and white kaolin (Figure 2B). The fossil fumaroles were located around the rims of two pyroclastic cones on the northern volcanic flank. Here pyroclastic rock had been altered to soft red, brown, orange clay. A subsequent assessment of geothermal resources in 2010 located 11 fumaroles within the summit crater, crater wall and on flank eruption centres (Figure 2A–B) (Alexander and Ussher, 2011).

Studies at Longonot have since mainly focused on using the eruptive products to understand the petrogenesis of peralkaline magmas (Macdonald, 2012), the evolution of peralkaline systems (Macdonald et al., 2014) and the fractionation rates and magma storage times of magma (Rogers et al., 2004b). A magnetotelluric (MT) survey, conducted in 2010, measured resistivity at Longonot for geothermal prospecting and indicate the presence of a clay cap forming over a high temperature reservoir to the south of Longonot (Alexander and Ussher, 2011). Oxygen and hydrogen isotope compositions of geothermal fluids have been used to suggest that Longonot's geothermal reservoir is recharged from rainfall from the eastern rift shoulder, which possibly contrasts to Olkaria's reservoir, which may be recharged by Lake Naivasha (Alexander and Ussher, 2011).

Between 28 June 2004 – 20 March 2006, surface uplift of ~9 cm was detected at Longonot, measured using InSAR (Biggs et al., 2009b). No ground deformation was observed immediately prior to 2004, and no other geophysical measurements are available. After 2006, ground subsidence at a rate of -0.5 cm yr^{-1} was measured up to 2010, after which radar data is unavailable (Biggs et al, 2016). Elastic modelling based on both a spherical source (Mogi, 1958) and a horizontal penny-shaped crack (Fialko et al., 2001) both produced displacement patterns similar to the observed InSAR uplift and subsidence signals, showing that the deformation could be explained using either of these geometries (Biggs et al., 2009b). The penny-shaped crack model had slightly lower residuals, placing the uplift source at <4.5 km depth and the subsidence source at <2 km. Radial fringes on the uplift interferogram suggest a magmatic origin, but the presence of a shallow hydrothermal system at Longonot means that a volume change in a hydrothermal system cannot be discounted. However, the shallow source depth for the subsidence signal strongly indicates that it originated within the hydrothermal system. Based on these observations, it is probable that the hydrothermal system was perturbed by a deep magmatic injection in 2004 – 2006, heating the overlying boiling aquifer that ultimately led to ground subsidence.

The presence of these volcanoes, their calderas, pyroclastic deposits and geodetic signs of unrest strongly suggests that the Kenyan Rift is capable of producing large volcanic eruptions. There are few historical records of minor volcanism in Kenya, and there is no ground-based monitoring, nor any understanding of what the frequency and magnitude of past eruptions has been. Baseline records of diffuse degassing, for example, do not exist. Consequently, compared to other volcanic regions, the present-day magmatic processes in Kenya remains poorly recorded and the accompanying assessment of hazard and risk unquantified. Over 410,000 people live within 30 km of Longonot, and 8.7 million people within 100 km (Siebert et al., 2010). In a recent UN global assessment on volcanic hazard and risk, Longonot is shown to have insufficient data in the eruption record to adequately assess the hazard, and thus assessment of both hazard and risk are associated with large uncertainties. The high population exposure however suggests a risk level of II to III on a scale of risk levels from I-III (Brown et al., 2015).

3. Methods

3.1 Geological mapping and structural features

We used Advanced Spaceborne Thermal Emission and Reflection Radiometer (ASTER) and SPOT5 imagery to map structural features and the spatial extent of lava flows at Longonot, combined with information from the geological map of Dunkley et al. (1993). We used the ASTER Level 1B (radiance at sensor) product acquired on 6 August 2007 and SPOT5 multispectral 2.5 m resolution image acquired on 27 January 2010. We use the atmospheric correction FLAASH module in ENVI© v4.8 to retrieve spectral reflectance from radiance images (only visible near-infrared (VNIR) and short-wave infrared (SWIR) bands). To distinguish geological features, we applied interactive (false-colour-composite and histogram stretching) techniques to increase the contrast between units (Figure 3) (Vye-Brown et al., 2013). We also used pan-sharpening, band ratios and principal component analysis to increase the spectral contrast between specific absorption features (Rowan and Mars, 2003). The images were then layered over the SRTM and ASTER GDEM DEMs in ArcGIS© v10.0 and a geocoded and orthorectified version of the geological map of Dunkley et al. (1993). Errors depend on the spatial resolution of the image (2.5 – 15 m) and the manual error in identifying flows.

3.2 Soil CO survey

In November 2012, a soil CO_2 flux survey was carried out at Longonot volcano using the method of Hutchison et al (2015). We surveyed on days with stable and dry atmospheric conditions, measuring a total of 270 sites. CO_2 measurements were taken using a portable Li-COR LI-8100 automated soil CO_2 flux system analyser and a PP Systems EGM-4 Environmental Gas Monitor attached to a SRC-1 Soil Respiration Chamber. Both pieces of equipment use the accumulation chamber technique (Chiodini et al., 1998) to measure CO_2 efflux. They consist of an inverted chamber and an infrared gas analyser (IRGA) that measures both CO_2 concentration and flux. During a sample reading, the CO_2 gas diffuses into the accumulation chamber and is pumped into the IRGA, where the concentration is measured before being re-circulated back into the chamber. To minimize lateral diffusion of CO_2 in the soil, the chambers were placed on a soil collar that was inserted into the ground before the measurements were taken. To check that background variability was low and ensure consistency between instruments, multiple sequential readings or simultaneous measurements using the Li-COR and PP system were taken at a randomly-selected subset of sites. Variations were on the order of 10%–25% comparable with random error in natural emission rates (Carapezza and Granieri, 2004; Viveiros et al., 2010) and the stated precision of the instruments (5%–10%, Chiodini et al., 1998; Giammanco et al., 2007; Hutchison et al, 2015).

Sampling was conducted along transects (Figure 2C) that were chosen to cover recent structural features (e.g. pit crater and faults), identified by detailed mapping. Five transects cover the volcanic edifice (Figure 2C): A and B traverse up the modern trachyte cone, with B covering pyroclastic cones; transects C to D are located beyond the trachyte lava cone, and are perpendicular to recent volcano-tectonic or tectonic structural alignments. We also took measurements along the summit crater path, down the crater wall and along the perimeter of the crater floor, as fumaroles were detected in these locations by both Dunkley et al. (1993) and Alexander and Ussher (2011).

CO_2 flux populations were determined by probability distribution analysis using the Graphical Statistical Analysis (GSA) method of Sinclair (1974), described by Chiodini et al. (1998). The cumulative probability of CO_2 flux is plotted on a log scale - inflection points reflect the boundary between statistical lognormal populations and consequently, different flux sources (Figure. 4). The mean flux of each population and its corresponding 95% confidence limits were determined following the method of Sinclair (1974). Bimodal CO_2 flux distributions occur frequently at volcanic and hydrothermal settings (Mazot et al., 2013; Parks et al., 2013). The high flux source is often interpreted as originating from a relatively deep source of gas, such as a volcanic-hydrothermal system. The low flux population is generally attributed as background, resulting from biological activity in the soil (Chiodini et al., 2008; Chiodini et al., 1998; Giammanco et al., 2010).

Usually the Sequential Gaussian Simulation (sGs) method is used as a geostatistical approach to interpolate the spatial variability of soil CO_2 flux and to calculate the total volatile output (e.g. Parks et al, 2013; Hutchison et al, 2015). However, as the high flux values are restricted to isolated small areas, we estimate the total area to be degassing, and multiply this area by the mean high flux value, using maximum and minimum values to generate a range of possible estimates. Three high flux localities were identified: the crater wall, crater floor and pyroclastic cones (Figure 2). The area actively degassing at each locality was calculated individually using satellite imagery and evidence from fieldwork. The error in the flux rate is determined from the GSA probability distribution analysis, and estimates of the minimum and maximum plausible degassing area.

3.3 Composition of volcanic gases

Gas samples from high flux locations were collected for gas composition and carbon isotopic analysis (Hutchison et al, 2015). A T-connector was attached to the “out flow-line” between the Li-COR IRGA and the accumulation chamber, from which 12 ml of gas was extracted using a syringe 40 seconds into a two-minute analysis. Each sample was injected from the syringe into an evacuated glass vial through a pierceable butyl rubber septum and was analysed within three weeks of acquisition.

Loss of CO_2 is very low through the rubber septum (Tu et al., 2001), but the rate of helium loss may be higher due to its mobility. Gas composition and carbon isotope results were comparable between the two campaigns, even though one set of samples were analysed within a few days of sampling and the other within one month (W. Hutchison pers. comm.). Thus, we do not expect significant loss of volatiles through the rubber septum in our samples during storage.

Gas chemistry and carbon isotopes were measured at the Department of Earth & Planetary Sciences, University of New Mexico, using the methodology of Lee et al (2016). The bulk gas composition was determined with a Gow Mac gas chromatograph (GC) with discharge ionization detector (DID) and thermal conductivity detector (TCD) analyzers for CH_4, CO_2, H_2, and CO species, in tandem with a Pfeiffer quadrupole mass spectrometer (QMS) for Ar, He, N_2, and O_2 concentrations (De Moor et al., 2013; Fischer, 2008). The QMS analyses have a precision of <0.1%, except for the Helium, which has a precision of ±1% (de Moor et al, 2013). The analytical precision for the GC measurements is estimated at ±2% based on repeat measurements. The samples with the highest CO_2 concentration (i.e. lowest amount of air-derived CO_2) were selected for carbon isotope analysis. Carbon isotope data were collected with a Thermo-Finnigan Delta XP^{Plus} isotope ratio mass spectrometer. In total, seven samples were analysed for bulk gas composition, of which three were chosen for carbon isotope analysis.

4. Results

4.1 Geological map and structural alignments

Figure 2 presents a lava flow map delineating the spatial extent of individual trachyte lava flows (Lt^2). In contrast to the BGS map, this version largely excludes the pyroclastic cover ("from the Longonot Ash"). Lava flow edges are generally non-vegetated and well exposed in imagery. Even where edges of older flows are obscured, they could be identified using the enhanced imagery in conjunction with a DEM. Figure 3 shows a selection of images used to distinguish lavas, including principle component analysis and band ratios. We identify two subunits within the Lt^2 member and separate these into Lt^2a, Lt^2b, with Lt^2a at the stratigraphic base (Figure 3D).

Lava flow vents and pyroclastic cones are controlled by both rift-aligned faults and volcano-tectonic structures (Figure 2). These alignments are orientated NNW–SSE, parallel to the rift border faults, and perpendicular to the modern day extension orientation (109°; Figure 1). Consequently, the entire edifice has a NNW–SSE elongation – lava flows extend ~26 km in this orientation, but only ~10 km ENE–WSW.

Two lava flows (Lt^3) were emplaced following the "Longonot Ash" eruption on the north and southwestern flanks (Figure 2C). These units are dark grey/black trachytes with an a'a texture. There is minimal soil cover and vegetation on these units, consistent with the suggestion that they are recent deposits. The lava flow on the north flank is dated at 1863 BP, based on archeological evidence (Kimberley, 2011), but the age of the southwestern flow is unknown. Assuming that it is similar in age to the northern flow based on vegetation growth may be misleading. The southwestern flow originates from a fissure formed of six small craters, whilst the source of the northern flow can be traced to a single pyroclastic cone.

4.2 Soil CO_2

Soil CO_2 flux readings from Longonot volcano range from 0.13-99.9 g m^{-2} d^{-1} (Figure

9). Figure 4 is a probability plot of log-CO_2 flux values against cumulative probability and shows a bimodal distribution with one inflection point located at the 95^{th} percentile, indicating the presence of two CO_2 flux populations (A and B) with relative proportions of 5% and 95%. The gentle curvature of the inflection point suggests an overlap between the values in the two populations. The mean, 95% confidence interval and fraction of each population are reported in Table 1. Population A corresponds to 5% of the data with a mean flux value of 30 g m^{-2} d^{-1} (6.8 – 76 g m^{-2} d^{-1}; Figure 4 and Table 1). Population B represents 95% of the data with a mean flux of 0.86 g m^{-2} d^{-1} (values range from 0.3 – 2.3 g $m^{-2}d^{-1}$).

We interpret Population B as the background biogenic flux, supported by the observation that biogenic soil fluxes range between 0.2 – 20 g m^{-2} d^{-1}, and occasionally reach 40 – 50 g $m^{-2}d^{-1}$ in agricultural environments (Chiodini et al., 2008; Chiodini et al., 1998). Our survey area at Longonot was non-agricultural and in general lightly vegetated, and our sample sites were located in ash-rich sand and soils. In this region, our low flux measurements range from 0.3 – 2.3 g m^{-2} d^{-1}, within the range of biogenic CO_2 flux sources, even on the more densely-vegetated crater floor. In contrast, our high flux Population A has a mean value of 30 g m^{-2} d^{-1}, above typical biogenic values.

4.3 Degassing locations

We measured high soil CO_2 fluxes (Population A) at three localities: crater wall, pyroclastic cones, and the crater floor perimeter. The physical characteristics of these degassing sites vary (Figure 5A – C). On the crater wall, high fluxes were located at steaming fumaroles surrounded by highly altered rock less than 1m^2 in area. In contrast, degassing sites on the crater floor were richly vegetated, mildly altered, and lightly steaming. High flux readings on the pyroclastic cones were located on fossil fumaroles (non-steaming) and on altered red/brown soils, and were coincident with “geothermal grass” (Figure 5D; Lagat and Nakuru, 2011).

Longonot’s crater is 2 km in diameter with near-vertical walls at 50 – 150 m in height (Figure 6A). The lower part of the wall consists of dense trachyte lavas (Lt) and the upper part is composed of pyroclastic deposits from the “Longonot Ash” eruption (Lp^8). The base of the pyroclastic cover contains pumice lapilli and blocks, whilst the upper portion forms poorly consolidated ash layers. Fumaroles on the crater wall were located along fractures within the trachyte lavas, close to the pyroclastic-lava boundary. We also identified four further steaming fumaroles from the crater wall path, but were unable to access them (Figure 6C). The lithological change between the lavas and pyroclastic cover may represent migration pathways or barriers for fluid flow, and thus may control fumarole sites (Barde-Cabusson et al., 2009; Gudmundsson et al., 2002; Schöpa et al., 2011). From our observations, fumarole locations are likely controlled by structural features, such as fractures, but their proximity to the pyroclastic-lava boundary means that a lithological control cannot be discounted.

The crater floor is covered with mixed basalt and hawaiite lava flows (Lmx^2) that are blocky and a'a in texture. The lavas are >1 m in height and are densely vegetated by trees and bushes growing between blocks. The lavas are not overlain by soil, which is required to take gas measurements; furthermore, traversing the lavas is unfeasible. Therefore gas measurements were restricted to the crater floor perimeter, which has a soil-rich path that was 1 – 3 m wide. Fumaroles were located immediately adjacent to the path and likely mark the location of volcano-tectonic faults formed during the collapse of the pit crater. Our sampling extended 350 m around the crater floor; however, based on our observations we would expect fumaroles to exist along the whole perimeter. This view is supported by the fumaroles mapped by the BGS (Dunkley et al., 1993).

A series of three overlapping NNW – SSE aligned pyroclastic cones are situated on Longonot's northern flank (Figure 6B). The first cone is well defined, with a prominent circular crater 300 m diameter. The second cone has a small, shallow crater approximately 100 m diameter, but its deposits cover a larger area downslope. The third cone is perhaps better classified as a fissure as there is no clear ejected material on its flanks. It has a breached circular rim and is the source of a lava flow that extends NNW (Lt^3). High flux readings were located on the topographic rims of the upper two cones, but only on the western edges. The absence of active fumaroles and minor soil alteration leads us to assume that these are fossil fumaroles, which is in agreement with Dunkley et al. (1993).

The majority of the soil CO_2 flux measurements (95%) yielded values that fall within background biogenic values. The location and physical characteristics of these sites vary, from the modern trachyte cone to the flat-lying plains (Transects A-D; Figure 7). We see no variation in flux rates between sites that are covered with either relatively older or younger lava flows. At the end of Transect C, there is a hint that the soil CO_2 flux was systematically increasing, with some readings above background. These sample sites are progressively closer to the hypothesised caldera rim fault; it is possible therefore that these high flux measurements mark the location of the caldera ring faults.

4.4 Total CO_2 output at Longonot

To estimate total CO_2 emissions from Longonot, we estimate the total high flux degassing area across the crater wall, crater floor and pyroclastic cones. We then multiply the degassing area by our calculated average high flux value (30 g m^{-2} d^{-1}).

At the crater wall, we measured three fumaroles directly and observed four more from the crater rim. Assuming the fumaroles are all 1 x 1 m^2, our minimum degassing area estimate is 7 m^2. For the maximum area, we estimate that 1% of the crater wall is degassing (Figure 8). Given that the crater wall area is ~0.8 km^2, this equates to 8000 m^2, and a total CO_2 output of 0.2 – 240 kg d^{-1}.

We took 13 flux measurements along a 350 m section of the crater floor, and recorded high soil fluxes at seven lightly steaming fumaroles. These fumaroles were not evenly distributed along the perimeter, but instead were clustered. Our minimum estimate for the degassing is limited to our observations at ~7 m^2 (Figure 9). For our upper estimate, we assume that this section is representative of the entire perimeter and extrapolate, giving a total area of 100 m^2 and a total CO_2 output of 0.2 – 3.0 kg d^{-1}.

High fluxes were located on the pyroclastic cone rims, but only at <12% of all sample sites in this area. Our lower bound area is constrained at 10 m^2. We do not expect the rest of the pyroclastic cones to be degassing significantly, both from our field observations and those of Dunkley et al. (1993). Our maximum area estimate is the total area that encases the fossil fumaroles, ~500 m^2 (Figure 11) and so the total CO_2 output is estimated at 0.3 – 15 kg d^{-1}.

In total, we estimate an area of 24 – 8,600 m^2 is outgassing CO_2 at Longonot. Given that Population A degases at 30 g m^{-2} d^{-1}, we estimate that the edifice is emitting 0.7-258 kg d^{-1} CO_2, of which 93% originates from the crater wall (Table 2).

4.5 Gas composition

Bulk gas composition and carbon isotope values are reported in Table 3. All samples are contaminated by air, as indicated by O_2 and N_2 values of approximately 21% and 77% respectively, although CO_2 concentrations are an order of magnitude greater than atmospheric for the majority of samples. Typical high-temperature fumarolic gases have negligible O_2, and low N_2 values (Fischer, 2008). Air contamination may be a consequence of using an accumulation chamber rather than Giggenbach bottles for sampling, but air entrainment in fumarolic gases measured in near-surface soils has also previously been observed at some volcanoes in Kenya, including Longonot (Alexander and Ussher, 2011; Darling et al., 1995), and also at other volcanoes worldwide (Giammanco et al., 1997).

The ^{13}C values of fumaroles in this study range from -4.7 ‰ to -6.4 ‰ and are within the mantle component of the EARR and consistent with earlier measurements in the region (Figure 4b; Darling et al, 1995). Sample ER15.2 is isotopically lighter than the other two samples (<-6.4 ‰), which may indicate an element of bacterially produced CO_2 from the soil (Darling et al., 1995). The extrapolated magmatic “end member” for Longonot’s ^{13}C is likely to be between -3 ‰ and -4 ‰, consistent with values from across Kenya (Figure 4b; Darling et al., 1995).

5 Discussion

5.1 Structural control and source of CO_2 degassing

Diffuse degassing is an important outlet for magmatic and hydrothermal volatiles and occurs along permeable pathways, such as faults and fractures and through soils, hot and cold springs, lakes (Allard et al., 1991; Chiodini et al., 1998). Our results show that Longonot volcano is degassing 0.7-258 kg d^{-1} CO_2 to the atmosphere, mainly through crater wall structures. These high flux locations are controlled by volcano-tectonic and regional tectonic structures where fluids flow along faults and fractures that have a higher permeability compared to the surrounding rock (Arnórsson, (1995; Chesner and Rose, 1991). Topography or underlying fissures may control the fossil fumarole locations. Topography alters the stress field, where fluid flow is directed parallel to the minimum compressive stress along topographic highs, thus focusing fluid flow to crater rims (Acocella et al., 2006; Anderson, 1951; Schöpa et al., 2011). The log-probability plot shows the presence of two flux populations: a low flux population (Population B) interpreted as background, and a high flux population (Population A; Figure 4) interpreted as magmatic. The average high flux value of 30 g m^{-2} d^{-1} is low compared to other volcanoes such as Vulcano (Italy) that has an average rate up to 18,000 g $m^{-2}d^{-1}$ (Chiodini et al., 2008) or Fogo

(Azores) with an average rate up to 600 g $m^{-2}d^{-1}$ (Viveiros et al, 2008). Consequently, soil degassing is an effective technique to detect active faults and fractures at Longonot, similar to studies at Santorini and Etna volcanoes (Barberi and Carapezza, 1994; Giammanco et al., 1997).

The depleted upper mantle has $\delta^{13}C$ values of -5±1 ‰ (vs. PDB) based on a global data-set of MORB glasses (Marty and Zimmermann, 1999), fumarole gas discharges from Ol Doinyo Lengai, Tanzania have $\delta^{13}C$ of -2.4 to -4.0 ‰ (Fischer et al., 2009b), hot spring discharges from the Rungwe Volcanic region in Southern Tanzania range from -2.8 to -6.5 ‰ (Barry et al., 2013) and diffuse CO_2 emissions from the Lake Natron and Lake Magadi area have an extrapolated end-member $\delta^{13}C$ value of approximately -6 ‰ (Lee et al., 2016). Atmospheric values are -8.5 ‰ (Keeling and Whorf, 2005). Heavier and lighter $\delta^{13}C$ values (up to 0 ‰) are found in arc volcanoes and are due to the contribution of organic or carbonate derived carbon from the subducting slab (Oppenheimer et al., 2014; Sano and Marty, 1995) in continental rift settings, however, we expect values close to the upper mantle with possible influence of C derived from a plume component. The^{13}C composition of the gases ranges measured at Longonot range from -4.7 ‰ to -6.4 ‰ (Figure 4b) and falls within the range measured throughout the Kenyan Rift (KR) by Darling et al. (1995) who measured a $\delta^{13}C$ of -1.7 ‰ to -7.1 ‰, with an average of -3.7 ‰ (± 1.1 ‰). One sample from a fumarole at Longonot has a $\delta^{13}C$ of -4.0 ‰ and a helium isotope ratio (the ratio of helium isotopes in the sample relative to their ratio in air) R/R_A = 6.7 (Darling et al., 1995). Consequently, Darling et al. (1995) interpreted these data as evidence for a deep mantle source for Longonot's fumarolic gases, which is consistent with our interpretation (Figure 4b). Similar helium ratios (R/R_A = 5.5 – 8) and $\delta^{13}C$ values are found at the majority of fumaroles and springs associated with late-Quaternary silicic volcanoes in the Kenyan and Tanzania section of the rift (Barry et al., 2013; Darling et al., 1995), Ol Doinyo Lengai fumaroles (Fischer et al., 2009a; Teague et al., 2008), carbonatites in Tanzania and mantle xenoliths from the Chyulu Hills volcanic field (Hopp et al., 2007) and phenocrysts from the Rungwe volcanic region, southern Tanzania (Hilton et al., 2011).

5.2 Hydrothermal System

Circulation of hydrothermal fluids plays a key role in driving ground deformation at many calderas (Chiodini et al., 2003; Dzurisin et al., 2006; Hurwitz et al., 2007; Wicks et al., 1998) and numerical models highlight that even small changes in permeability and anisotropy of the host rock, and the depth and rate of hydrothermal fluid injection can lead to significant variations in ground surface displacement and degassing (Hurwitz et al., 2007). Longonot's geothermal reservoir is liquid-dominated, comprising a boiling aquifer with a vapour- dominated cap with temperatures of 250 – 300 °C (Alexander and Ussher, 2011). The spatial distribution of high CO_2 fluxes demonstrates that volcano-tectonic structures control near-surface permeability at Longonot but it is unclear whether these features extend into the reservoir itself.

Magmatic volatiles dissolve into hydrothermal systems and outgassing measurements at the surface may be lower than expected at volcanoes with mature hydrothermal systems (Werner et al., 2012). Carbon isotope fractionation occurs during the transport of volatiles by aqueous fluids and by calcite precipitation (Barry et al., 2014; Barry et al., 2013; Ray et al., 2009) and the latter process in particular is highly temperature dependent (Barry et al., 2014; Hoefs, 2010). Calcite-anhydrite dissolution and precipitation in geothermal reservoirs depend on pCO_2 variations (Chiodini et al., 2007; Marini and Chiodini, 1994), with a reduction in this value leading to sealing of the system by anhydrite precipitation, as seen at Campi Flegrei (Chiodini et al., 2007). In areas of high permeability, sustained CO_2 fluxes and heat can maintain lower pCO_2 values, minimizing precipitation and encouraging fluid flow and volatile release. Based on its proximity and general similarities in host rock composition (Macdonald et al., 2008), the Longonot hydrothermal system is considered comparable to that of Olkaria, where reservoir CO_2 concentration is largely controlled by a flux from a magmatic heat source and CO_2 is removed via calcite precipitation within the aquifer (Karingithi et al., 2010). Thus, we infer that a proportion of CO_2 from the magma source at Longonot is precipitated out of the system.

5.3 Sources of CO_2 in the East African Rift

The total estimated CO_2 degassing at Longonot is <0.3 t d^{-1} (0.1 kt yr^{-1}) and is small compared to measurements made at other active volcanoes. The only other volcanoes with CO_2 flux estimates in East Africa are Ol Doinyo Lengai Volcano, Tanzania, with a flux of ~100 t d^{-1} (36 kt yr^{-1}) (Koepenick et al., 1996) and Aluto Volcano, Ethiopia. At Aluto, measurements were made of the Artu Jawe fault zone, a major structural pathway for fluid flow, giving an estimated flux of 57 t d^{-1} (21 kt yr^{-1}) of CO_2 (Hutchison et al., 2015). However, the Artu Jawe represents a small proportion of the total area of hydrothermal alteration, and extrapolating gives a total degassing flux of 250-500 t d^{-1} (90-180 kt yr^{-1}) for the whole of Aluto's edifice.

These three volcanoes have very different eruption records. Ol Doinyo Lengai is an actively erupting volcano, so a high CO_2 flux is not surprising. Longonot had a historically-recorded eruption in 1863, but although Aluto has clearly experienced many eruptions during the Holocene, none have been historically observed (Hutchison et al, in review), suggesting that the last eruption occurred prior to that at Longonot. In terms of unrest, both Longonot and Aluto have experienced significant ground deformation during the ~20 year geodetic record (Biggs et al., 2009b; Biggs et al., 2011b; Biggs et al., 2016; *Hutchison et al, accepted)*, but the deformation at Aluto is both larger magnitude and more persistent than that at Longonot. Although in both cases, the degassing patterns are controlled by structural features, the total CO_2 flux at Aluto is orders of magnitude higher, and the spatial patterns are quite different; at Aluto degassing extends along and beyond the 8 km-wide ring fault, whereas at Longonot, the high flux sites were observed either inside the ~3 km wide summit crater or at parasitic cones less than a kilometer away. Taken together, these differences in the patterns and magnitudes of both deformation and degassing suggest a larger volume of magma is currently stored under Aluto than under Longonot.

Recent estimates of degassing along tectonic faults in rift basins are orders of magnitudes larger than any of the estimates of degassing from rift volcanoes. Estimates from the Magadi basin, Kenya and Natron basin, Tanzania, located <200 km south of Longonot, are 2700 ± 800 t d^{-1} (980 kt yr^{-1}) and 570 ± 160 t d^{-1} (210 kt yr^{-1}) respectively (Lee et al., 2016). If one assumes that this can be extrapolated to the entire length of the eastern branch of the East African Rift, this is 71 ± 33 Mt yr^{-1}, equivalent to the entire mid-ocean ridge system. The high CO_2 fluxes away from volcanic edifices is consistent with the idea that magma flux is continuous along the rift and a signficiant proportion is stored or intruded away from the volcanic centres. High density, crystallised intrusions are observed in both the Main Ethiopian Rift (Keranen et al., 2004b) and Kenyan Rifts (Swain, 1992) and comparison between geodetic constraints on dyke intrusions and the volumes of lava flow fields in Afar constrain the intrusive-extrusive ratio for recent events at 5 – 10:1 (Ferguson et al., 2010).

6. Conclusions

This study shows that CO_2 degassing at Longonot was <0.3 t d^{-1} (0.1 kt yr^{-1}) [1] in November 2012. We show that volcanic structural faults and fractures control degassing pathways, with the majority of outgassing emanating from the crater wall. The chemical composition of fumarolic gases is heavily contaminated by air, but carbon isotope data imply a mantle source for the carbon, with a minor addition of organic carbon from the shallow hydrothermal system. The total flux is less than that observed at other volcanoes within the rift, such as Aluto and Ol Doinyo Lengai and significantly less than the flux from nearby basins.

Acknowledgements

ER was supported by a NERC Algorithm studentship and fieldwork grants from National Geographic and GRSG. ER, JB, ME and CV-B belong to the NERC Centre for the Observation and Modeling of Earthquakes, Volcanoes and Tectonics and JB, ME and CV-B were funded by the NERC RiftVolc Grant NE/L013932/1. Gas analyses at the University of New Mexico were partially supported by the Volcanic and Geothermal Volatiles laboratory and by NSF grant (EAR-1113066) to TF. We thank Bruce Mutagi, James Hammond, Will Hutchison and Frank Chetchet for their help in the field.

References

Abebe, B., Acocella, V., Korme, T. and Ayalew, D., 2007. Quaternary faulting and volcanism in the Main Ethiopian Rift. J. Afri. Earth Sci., 48(2-3): 115 - 124.

Acocella, V., Neri, M. and Scarlato, P., 2006. Understanding shallow magma emplacement at volcanoes: orthogonal feeder dikes during the 2002--2003 Stromboli (Italy) eruption. Geophysical Research Letters, 33(17): L17310.

Aiuppa, A., Caleca, A., Federico, C., Gurrieri, S. and Valenza, M., 2004. Diffuse degassing of carbon dioxide at Somma--Vesuvius volcanic complex (Southern Italy) and its relation with regional tectonics. Journal of Volcanology and Geothermal Research, 133(1): 55-79.

Alexander, K.B. and Ussher, G., 2011. Geothermal resource assessment for Mt. Longonot, central Rift Valley, Kenya. Geothermal Resources Council Transactions, 35: 1147-1154.

Allard, P., Carbonnelle, J., Dajlevic, D., Le Bronec, J., Morel, P., Robe, M.C., Maurenas, J., Faivre-Pierret, R., Martin, D., Sabroux, J. and others, 1991. Eruptive and diffuse emissions of CO_2 from Mount Etna. Nature, 351(6325): 387-391.

Anderson, E.M., 1951. The dynamics of faulting and dyke formation with application to Britain (2nd edition). Oliver and Boyd, Edinburgh.

Armannsson, H., Fridriksson, T and Kristjánsson, B.R., 2005. CO_2 emissions from geothermal power plants and natural geothermal activity in Iceland. Geothermics, 34(3): 286-296.

Arnórsson, S., 1995. Geothermal systems in Iceland: Structure and conceptual models -- I. High-temperature areas. Geothermics, 24(5): 561-602.

Baptiste, V., Tommasi, A., Vauchez, A., Demouchy, S. and Rudnick, R.L., 2015. Deformation, hydration, and anisotropy of the lithospheric mantle in an active rift: Constraints from mantle xenoliths from the North Tanzanian Divergence of the East African Rift. Tectonophysics, 639: 34-55.

Barberi, F. and Carapezza, M.L., 1994. Helium and CO_2 soil gas emission from Santorini (Greece). Bulletin of Volcanology, 56(5): 335-342.

Barde-Cabusson, S., Finizola, A., Revil, A., Ricci, T., Piscitelli, S., Rizzo, E., Angeletti, B., Balasco, M., Bennati, L. and Byrdina, S., 2009. New geological insights and structural control on fluid circulation in La Fossa cone (Vulcano, Aeolian Islands, Italy). Journal of Volcanology and Geothermal Research, 185(3): 231-245.

Barry, P., Hilton, D., Füri., E, Halldórsson., SA and Grönvold., K, 2014. Carbon isotope and abundance systematics of Icelandic geothermal gases, fluids and subglacial basalts with implications for mantle plume-related CO_2 fluxes. Geochimica et Cosmochimica Acta, 134: 74-99.

Barry, P.H., Hilton, D.R., Fischer, T.P., de Moor, J.M., Mangasini, F. and Ramirez, C., 2013. Helium and carbon isotope systematics of cold ``mazuku'' CO_2 vents and hydrothermal gases and fluids from Rungwe Volcanic Province, southern Tanzania. Chemical Geology, 339: 141-156.

Behn, M.D., Conrad, C.P. and Silver, P.G., 2004. Detection of upper mantle flow associated with the African Superplume. Earth and Planetary Science Letters, 224(3): 259-274.

Belachew, M., Ebinger, C., Coté, D., Keir, D., Rowland, J.V., Hammond, J.O.S. and Ayele, A., 2011. Comparison of dike intrusions in an incipient seafloor-spreading segment in Afar, Ethiopia: Seismicity perspectives. Journal of Geophysical Research, 116(B6).

Bergfeld, D., Goff, F. and Janik, C.J., 2001. Elevated carbon dioxide flux at the Dixie Valley geothermal field, Nevada; relations between surface phenomena and the geothermal reservoir. Chemical Geology, 177(1): 43-66.

Biggs, J., Amelung, F., Gourmelen, N., Dixon, T. and Kim, S., 2009a. InSAR observations of 2007 Tanzania rifting episode reveal mixed fault and dyke extension in an immature continental rift. Geophysical Journal International, 179(1): 549-558.

Biggs, J., Anthony, E.Y. and Ebinger, C.J., 2009b. Multiple inflation and deflation events at Kenyan volcanoes, East African Rift. Geology, 37(11): 979-982.

Biggs, J., Bastow, I.D., Keir, D. and Lewi, E., 2011a. Pulses of deformation reveal frequently recurring shallow magmatic activity beneath the Main Ethiopian Rift. Geochemistry Geophysics Geosystems, 12.

Biggs, J., Bastow, I.D., Keir, D. and Lewi, E., 2011b. Pulses of deformation reveal frequently recurring shallow magmatic activity beneath the Main Ethiopian Rift. Geochemistry, Geophysics, Geosystems, 12: 10.

Biggs, J., Chivers, M. and Hutchinson, M.C., 2013a. Surface deformation and stress interactions during the 2007-2010 sequence of earthquake, dyke intrusion and eruption in northern Tanzania. Geophysical Journal International, 195(1): 16-26.

Biggs, J., Chivers, M. and Hutchinson, M.C., 2013b. Surface deformation and stress interactions during the 2007--2010 sequence of earthquake, dyke intrusion and eruption in northern Tanzania. Geophysical Journal International, 195(1): 16-26.

Biggs, J., Robertson, E. and Cashman, K., 2016. The lateral extent of volcanic interactions during unrest and eruption. Nature Geoscience.

Biggs, J., Robertson, E. and Mace, M., 2013c. ISMER--Active Magmatic Processes in the East African Rift: A Satellite Radar Perspective, Remote Sensing Advances for Earth System Science. Springer, pp. 81-91.

Brombach, T. and Hunziker, J.C., 2001. Soil diffuse degassing and thermal energy fluxes from the Southern Lakki plain, Nisyros (Greece). Geophysical Research Letters, 28(1): 69-72.

Brown, S.K., Sparks, R.S.J., Mee, K., Ilyinskaya, E., Jenkins S., Loughlin, S.C. and Vye-Brown, C., 2015. Regional and country profiles of volcanic hazard and risk. Report IV of the GVM/IAVCEI contribution to the UN-ISDR Global Assessment Report on Disaster Risk Reduction 2015,

Calais, E., d'Oreye, N., Albaric, J., Deschamps, A., Delvaux, D., Déverchére, J., Ebinger, C., Ferdinand, R., Kervyn, F., Macheyeki, A., Oyen, A., Perrot, J., Saria, E., Smets, B., Stamps, D.S. and Wauthier, C., 2008. Strain accommodation by slow slip and dyking in a youthful continental rift, East Africa. Nature Geoscience, 456: 783-787.

Carapezza M.L., Granieri D., 2004, CO_2 soil flux at Vulcano (Italy): Comparison between active and passive methods: Applied Geochemistry, 19, 73–88,.

Cardellini, C., Chiodini, G. and Frondini, F., 2003. Application of stochastic simulation to CO_2 flux from soil: Mapping and quantification of gas release. Journal of Geophysical Research, 108(B9): 2425.

Castillo, P.R., Hilton, D.R. and Halldórsson, S.A., 2014. Trace element and Sr-Nd-Pb isotope geochemistry of Rungwe Volcanic Province, Tanzania: implications for a Superplume source for East Africa Rift magmatism. Frontiers in Earth Science, 2: 21.

Chesley, J.T., Rudnick, R.L. and Lee, C.-T., 1999. Re-Os systematics of mantle xenoliths from the East African Rift: Age, structure, and history of the Tanzanian craton. Geochimica et Cosmochimica Acta, 63(7): 1203-1217.

Chesner, C.A. and Rose, W.I., 1991. Stratigraphy of the Toba tuffs and the evolution of the Toba caldera complex, Sumatra, Indonesia. Bulletin of Volcanology, 53(5): 343-356.

Chiodini, G., Baldini, A., Barberi, F., Carapezza, M., Cardellini, C., Frondini, F., Granieri, D., Ranaldi, M. and others, 2007. Carbon dioxide degassing at Latera caldera (Italy): Evidence of geothermal reservoir and evaluation of its potential energy. Journal of Geophysical Research, 112(B12204).

Chiodini, G., Caliro, S., Cardellini, C., Avino, R., Granieri, D. and Schmidt, A., 2008. Carbon isotopic composition of soil CO_2 efflux, a powerful method to discriminate different sources feeding soil CO_2 degassing in volcanic-hydrothermal areas. Earth and Planetary Science Letters, 274(3): 372-379.

Chiodini, G., Cioni, R., Guidi, M., Raco, B. and Marini, L., 1998. Soil CO_2 flux measurements in volcanic and geothermal areas. Applied Geochemistry, 13(5): 543-552.

Chiodini, G., Frondini, F., Cardellini, C., Granieri, D., Marini, L. and Ventura, G., 2001. CO_2 degassing and energy release at Solfatara volcano, Campi Flegrei, Italy. Journal of Geophysical Research, 106(B8): 16213-16216.

Chiodini, G., Frondini, F. and Raco, B., 1996. Diffuse emission of CO_2 from the Fossa crater, Vulcano Island (Italy). Bulletin of Volcanology, 58(1): 41-50.

Chiodini, G., Todesco, M., Caliro, S., Del Gaudio, C., Macedonio, G. and Russo, M., 2003. Magma degassing as a trigger of bradyseismic events: The case of Phlegrean Fields (Italy). Geophysical Research Letters, 30(8).

Clarke, M.C.G., Woodhall, D.G., Allen, D. and Darling, G., 1990. Geology, volcanological and hydrological controls on the occurrence of geothermal activity in the area surrounding Lake Naivasha, Kenya, British Geological Survey and Kenyan Ministry of Energy.

Darling, W., Griesshaber, E., Andrews, J., Armannsson, H. and O'Nions, R., 1995. The origin of hydrothermal and other gases in the Kenya Rift Valley. Geochimica et cosmochimica acta, 59(12): 2501-2512.

Dawson, J.B., Pinkerton, H., Pyle, D.M. and Nyamweru, C., 1994. June 1993 eruption of Oldoinyo Lengai, Tanzania: Exceptionally viscous and large carbonatite lava flows and evidence for coexisting silicate and carbonate magmas. Geology, 22: 799-+.

De Moor, J., Fischer, T., Sharp, Z., Hilton, D., Barry, P., Mangasini, F. and Ramirez, C., 2013. Gas chemistry and nitrogen isotope compositions of cold mantle gases from Rungwe Volcanic Province, southern Tanzania. Chemical Geology, 339: 30-42.

Deans, T. and Roberts, B., 1984. Carbonatite tuffs and lava clasts of the Tinderet foothills, western Kenya: a study of calcified natrocarbonatites. Journal of the Geological Society, 141(3): 563-580.

Dereinda, F.H., 2008. CO_2 Emissions from the Krafla Geothermal Area, Iceland. Orkustofnun.

Dunkley, P.N., Smith, M., Allen, D.J. and Darling, W.G., 1993. The geothermal activity and geology of the northern sector of the Kenya Rift Valley, British Geological Survey Research Report SC/93/1.

Dzurisin, D., Lisowski, M., Wicks, C.W., Poland, M.P. and Endo, E.T., 2006. Geodetic observations and modeling of magmatic inflation at the Three Sisters volcanic center, central Oregon Cascade Range, USA. Journal of Volcanology and Geothermal Research, 150(1-3): 35-54.

Ebinger, C.J. and Sleep, N., 1998. Cenozoic magmatism throughout East Africa resulting from impact of a single plume. Nature, 395(6704): 788-791.

Fialko, Y., Khazan, Y. and Simons, M., 2001. Deformation due to a pressurized horizontal circular crack in an elastic half-space, with applications to volcano geodesy. Geophysical Journal International, 146(1): 181-190.

Fischer, T., Burnard, P., Marty, B., Hilton, D., Füri, E, Palhol, F., Sharp, Z. and Mangasini, F., 2009a. Upper-mantle volatile chemistry at Oldoinyo Lengai volcano and the origin of carbonatites. Nature, 459(7243): 77-80.

Fischer, T.P., 2008. Fluxes of volatiles (H_2O, CO_2, N_2, Cl, F) from arc volcanoes. Geochemical Journal, 42(1): 21-38.

Fischer, T.P., Burnard, P., Marty, B., Hilton, D.R., Füri, E., Palhol, F., Sharp, Z.D. and Mangasini, F., 2009b. Upper-mantle volatile chemistry at Oldoinyo Lengai volcano and the origin of carbonatites. Nature. 459: 77-80.

Fournier, T., Pritchard, M. and Riddick, S., 2010a. Duration, magnitude, and frequency of subaerial volcano deformation events: New results from Latin America using InSAR and a global synthesis. Geochemistry, Geophysics, Geosystems, 11(1): Q01003.

Fournier, T.J., Pritchard, M.E. and Riddick, S.N., 2010b. Duration, magnitude, and frequency of subaerial volcano deformation events: New results from Latin America using InSAR and a global synthesis. Gcubed, 11: Q01003.

Fridriksson, T., Padrón, E., Óskarsson, F., & Pérez, N. M. (2016). Application of diffuse gas flux measurements and soil gas analysis to geothermal exploration and environmental monitoring: Example from the Reykjanes geothermal field, SW Iceland. *Renewable Energy*, *86*, 1295-1307

Giammanco, S., Bellotti, F., Groppelli, G. and Pinton, A., 2010. Statistical analysis reveals spatial and temporal anomalies of soil CO_2 efflux on Mount Etna volcano (Italy). Journal of Volcanology and Geothermal Research, 194(1): 1-14.

Giammanco, S., Gurrieri and Valenza, M., 1997. Soil CO_2 degassing along tectonic structures of Mount Etna (Sicily): the Pernicana fault. Applied Geochemistry, 12(4): 429-436.

Grandin, R., Socquet, A., Binet, R., Klinger, Y., Jacques, E., de Chabalier, J.-B., King, G.C.P., Lasserre, C., Tait, S. and Tapponnier, P., 2009. September 2005 Manda Hararo-Dabbahu rifting event, Afar (Ethiopia): constraints provided by geodetic data. Journal of Geophysical Research, 114(B8).

Granieri, D., Avino, R. and Chiodini, G., 2010. Carbon dioxide diffuse emission from the soil: ten years of observations at Vesuvio and Campi Flegrei (Pozzuoli), and linkages with volcanic activity. Bulletin of Volcanology, 72(1): 103-118.

Gudmundsson, A., Fjeldskaar, I. and Brenner, S.L., 2002. Propagation pathways and fluid transport of hydrofractures in jointed and layered rocks in geothermal fields. Journal of Volcanology and Geothermal Research, 116(3): 257-278.

Hammond, J.O.S., Kendall, J.-M., Stuart, G.W., Keir, D., Ebinger, C., Ayele, A. and Belachew, M., 2011. The nature of the crust beneath the Afar triple junction: evidence from receiver functions. Geochemistry, Geophysics, Geosystems, 12(12): Q12004.

Hernández, P. A., Pedro A., Perez, N., Fridriksson, T., Egbert, J., Ilyinskaya, E., Thárhallson., A., Ívarsson, G., Gíslason G., Gunnarsson, I., Jónsson, B. and others, 2012. Diffuse volcanic degassing and thermal energy release from Hengill volcanic system, Iceland. Bulletin of Volcanology, 74(10): 2435-2448.

Hilton, D., Halldórsson, SA, Barry, P., Fischer, T., de Moor, J., Ramirez, C., Mangasini, F. and Scarsi, P., 2011. Helium isotopes at Rungwe Volcanic Province, Tanzania, and the origin of East African Plateaux. Geophysical Research Letters, 38(21): L21304.

Hoefs, J., 2010. Geochemical fingerprints: a critical appraisal. European Journal of Mineralogy, 22(1): 3-15.

Hopp, J., Trieloff, M. and Altherr, R., 2007. Noble gas compositions of the lithospheric mantle below the Chyulu Hills volcanic field, Kenya. Earth and Planetary Science Letters, 261(3): 635-648.

Hudgins, T., Mukasa, S., Simon, A., Moore, G. and Barifaijo, E., 2015. Melt inclusion evidence for CO_2 -rich melts beneath the western branch of the East African Rift: implications for long-term storage of volatiles in the deep lithospheric mantle. Contributions to Mineralogy and Petrology, 169(5): 1-18.

Hui, H., Peslier, A.H., Rudnick, R.L., Simonetti, A. and Neal, C.R., 2015. Plume-cratonic lithosphere interaction recorded by water and other trace elements in peridotite xenoliths from the Labait volcano, Tanzania. Geochemistry, Geophysics, Geosystems.

Hurwitz, S., Christiansen, L.B. and Hsieh, P.A., 2007. Hydrothermal fluid flow and deformation in large calderas: Inferences from numerical simulations. Journal of Geophysical Research, 112(B2): B02206.

Hutchison, W., Biggs, J., Mather, T.A., Pyle, D.M., Lewi, E., Yirgu. G., Caliro, S., Chiodini, G., Clor. L.E., & Fischer, T. accepted Causes of unrest at silicic calderas in the East African Rift: new constraints from InSAR and soil-gas chemistry at Aluto volcano, Ethiopia. Geochemistry, Geophysics, Geosystems

Hutchison, W., Mather, T.A., Pyle, D.M., Biggs, J. and Yirgu, G., 2015. Structural controls on fluid pathways in an active rift system: A case study of the Aluto volcanic complex. Geosphere, 11(3): 542-562.

Karingithi, C.W., Arnórsson, S. and Grönvold, K., 2010. Processes controlling aquifer fluid compositions in the Olkaria geothermal system, Kenya. Journal of Volcanology and Geothermal Research, 196(1): 57-76.

Keeling, C.D. and Whorf, T.P., 2005. Atmospheric CO_2 records from sites in the SIO air sampling network. Trends: a compendium of data on global change: 16-26.

Keranen, K., Klemperer, S.L. and Gloaguen, R., 2004a. Three-dimensional seismic imaging of a protoridge axis in the Main Ethiopian rift. Geology, 32: 949-952.

Keranen, K., Klemperer, S.L., Gloaguen, R. and Group, E.W., 2004b. Three-dimensional seismic imaging of a protoridge axis in the Main Ethiopian rift. Geology, 32(11): 949-952.

Kling, G.W., Clark, M.A., Wagner, G.N., Compton, H.R., Humphrey, A.M., Devine, J.D., Evans, W.C., Lockwood, J.P., Tuttle, M.L. and Koenigsberg, E.J., 1987. The 1986 Lake Nyos gas disaster in Cameroon, West Africa. Science, 236(4798): 169-175.

Koepenick, K.W., Brantley, S.L., Thompson, J.M., Rowe, G.L., Nyblade, A.A. and Moshy, C., 1996. Volatile emissions from the crater and flank of Oldoinyo Lengai volcano, Tanzania. Journal of Geophysical Research, 101: 13819-13830.

Lagat, J. and Nakuru, K., 2011. Geothermal surface exploration approach: case study of Menengai geothermal field, Kenya, Proceedings, Kenya Geothermal Conference 2011 Kenyatta International Conference Centre Nairobi.

Lee, H., Muirhead, J.D., Fischer, T.P., Ebinger, C.J., Kattenhorn, S.A., Sharp, Z.D. and Kianji, G., 2016. Massive and prolonged deep carbon emissions associated with continental rifting. Nature Geoscience. 9 145-149.

Lewicki, J.L. and Oldenburg, C.M., 2004. Strategies for detecting hidden geothermal systems by near-surface gas monitoring. Lawrence Berkeley National Laboratory, LBNL-56895.

Macdonald, R., 2012. Evolution of peralkaline silicic complexes: Lessons from the extrusive rocks. Lithos, 152: 11-22.

Macdonald, R., Bagiński., B. and Upton, B.G.J., 2014. The volcano--pluton interface; The Longonot (Kenya) and Kungnat (Greenland) peralkaline complexes. Lithos, 196: 232-241.

Macdonald, R., Belkin, H.E., Fitton, J.G., Rogers, N.W., Nejbert, K., Tindle, A.G. and Marshall, A.S., 2008. The roles of fractional crystallization, magma mixing, crystal mush remobilization and volatile--melt interactions in the genesis of a young basalt--peralkaline rhyolite suite, the Greater Olkaria Volcanic Complex, Kenya Rift Valley. Journal of Petrology, 49(8): 1515-1547.

Macdonald, R., Kjarsgaard, B.A., Skilling, I.P., Davies, G.R., Hamilton, D.L. and Black, S., 1993. Liquid immiscibility between trachyte and carbonate in ash flow tuffs from Kenya. Contributions to Mineralogy and Petrology, 114(2): 276-287.

Macdonald, R. and Scaillet, B., 2006. The central Kenya peralkaline province: Insights into the evolution of peralkaline salic magmas. Lithos, 91(1-4): 59-73.

Marini, L. and Chiodini, G., 1994. The role of carbon dioxide in the carbonate-evaporite geothermal systems of Tuscany and Latium (Italy). Acta Vulcanol, 5: 95-104.

Marty, B. and Zimmermann, L., 1999. Volatiles (He, C, N, Ar) in mid-ocean ridge basalts: Assesment of shallow-level fractionation and characterization of source composition. Geochimica et Cosmochimica Acta, 63(21): 3619-3633.

Mazot, A., Smid, E.R., Schwendenmann, L., Delgado-Granados, H. and Lindsay, J., 2013. Soil CO_2 flux baseline in an urban monogenetic volcanic field: the Auckland Volcanic Field, New Zealand. Bulletin of Volcanology, 75(11): 1-9.

Mogi, K., 1958. Relations between the eruptions of various volcanoes and the deformations of the ground surfaces around them. Bulletin of the Earthquake Research Institute Tokyo, 36(2): 99-134.

Nobile, A., Pagli, C., Keir, D., Wright, T.J., Ayele, A., Ruch, J. and Acocella, V., 2012. Dike-fault interaction during the 2004 Dallol intrusion at the northern edge of the Erta Ale Ridge (Afar, Ethiopia). Geophysical Research Letters, 39(19): L19305.

Notsu, K., Sugiyama, K., Hosoe, M., Uemura, A., Shimoike, Y., Tsunomori, F., Sumino, H., Yamamoto, J., Mori, T. and Hernández., PA, 2005. Diffuse CO_2 efflux from Iwojima volcano, Izu-Ogasawara arc, Japan. Journal of Volcanology and Geothermal Research, 139(3): 147-161.

Omenda, P.A., 1998. The geology and structural controls of the Olkaria geothermal system, Kenya. Geothermics, 27(1): 55-74.

Oppenheimer, C., Fischer, T. and Scaillet, B., 2014. Volcanic degassing: process and impact, Treatise on Geochemistry (Second Edition) Vol. 4, pp. 111-179.

Pagli, C., Wright, T.J., Ebinger, C.J., Yun, S.-H., Cann, J.R., Barnie, T. and Ayele, A., 2012. Shallow axial magma chamber at the slow-spreading Erta Ale Ridge. Nature Geoscience, 5(4): 284-288.

Pallister, J.S., McCausland, W.A., Jónsson, S., Lu, Z., Zahran, H.M., El Hadidy, S., Aburukbah, A., Stewart, I.C.F., Lundgren, P.R. and White, R.A., 2010. Broad accommodation of rift-related extension recorded by dyke intrusion in Saudi Arabia. Nature Geoscience, 3(10): 705-712.

Parks, M.M., Caliro, S., Chiodini, G., Pyle, D.M., Mather, T.A., Berlo, K., Edmonds, M., Biggs, J., Nomikou, P. and Raptakis, C., 2013. Distinguishing contributions to diffuse CO_2 emissions in volcanic areas from magmatic degassing and thermal decarbonation using soil gas ^{222}Rn-^{13}C systematics: Application to Santorini volcano, Greece. Earth and Planetary Science Letters, 377: 180-190.

Pik, R., Marty, B. and Hilton, D., 2006. How many mantle plumes in Africa? The geochemical point of view. Chemical geology, 226(3): 100-114.

Ray, M.C., Hilton, D.R., Muñoz, o., Jorge, Fischer, T.P. and Shaw, A.M., 2009. The effects of volatile recycling, degassing and crustal contamination on the helium and carbon geochemistry of hydrothermal fluids from the Southern Volcanic Zone of Chile. Chemical Geology, 266(1): 38-49.

Riaroh, D. and Okoth, W., 1994. The geothermal fields of the Kenya rift. Tectonophysics, 236(1-4): 117-130.

Ridolfi, F., Renzulli, A., Macdonald, R. and Upton, B.G.J., 2006. Peralkaline syenite autoliths from Kilombe volcano, Kenya Rift Valley: evidence for subvolcanic interaction with carbonatitic fluids. Lithos, 91(1): 373-392.

Ritsema, J., Ni, S., Helmberger, D.V. and Crotwell, H.P., 1998. Evidence for strong shear velocity reductions and velocity gradients in the lower mantle beneath Africa. Geophysical Research Letters, 25(23): 4245-4248.

Rogers, N.W., Evans, P.J., Blake, S., Scott, S.C. and Hawkesworth, C.J., 2004a. Rates and timescales of fractional crystallization from ^{238}U–^{230}Th–^{226}Ra disequilibria in trachyte lavas from Longonot volcano, Kenya. Journal of Petrology, 45(9): 1747-1776.

Rogers, N.W., Evans, P.J., Blake, S., Scott, S.C. and Hawkesworth, C.J., 2004b. Rates and timescales of fractional crystallization from ^{238}U-^{230}Th-^{226}Ra disequilibria in trachyte lavas from Longonot volcano, Kenya. Journal of Petrology, 45(9): 1747.

Rooney, T.O., Herzberg, C. and Bastow, I.D., 2012. Elevated mantle temperature beneath East Africa. Geology, 40(1): 27-30.

Rowan, L.C. and Mars, J.C., 2003. Lithologic mapping in the Mountain Pass, California area using advanced spaceborne thermal emission and reflection radiometer (ASTER) data. Remote Sensing of Environment, 84(3): 350-366.

Rudnick, R.L. and McDonough, W.F.a.C., B.W., 1993. Carbonatite metasomatism in the northern Tanzanian mantle: petrographic and geochemical characteristics. Earth and Planetary Science Letters, 114(4): 463-475.

Sano, Y. and Marty, B., 1995. Origin of carbon in fumarolic gas from island arcs. Chemical Geology, 119(1): 265-274.

Schöpa, A., Pantaleo, M. and Walter, T., 2011. Scale-dependent location of hydrothermal vents: Stress field models and infrared field observations on the Fossa Cone, Vulcano Island, Italy. Journal of Volcanology and Geothermal Research, 203(3): 133-145.

Scott, S.C., 1980. The geology of Longonot volcano, Central Kenya: a question of volumes. Philosophical Transactions of the Royal Society of London. Series A, Mathematical and Physical Sciences, 296(1420): 437-465.

Scott, S.C. and Skilling, I.P., 1999. The role of tephrachronology in recognizing synchronous caldera-forming events at the Quaternary volcanoes

Longonot and Suswa, south Kenya Rift. Geological Society Special Publications, 161(1): 47-67.

Siebert, L., Simkin, T. and Kimberly, P., 2010. Volcanoes of the World. University of California Press.

Sinclair, A.J., 1974. Selection of threshold values in geochemical data using probability graphs. Journal of Geochemical Exploration, 3(2): 129-149.

Sparks, R., 2003. Forecasting volcanic eruptions. Earth and Planetary Science Letters, 210(1): 1-15.

Stamps, D., Flesch, L., Calais, E. and Ghosh, A., 2014. Current kinematics and dynamics of Africa and the East African Rift System. Journal of Geophysical Research: Solid Earth, 119(6): 5161-5186.

Swain, C.J., 1992. The Kenya rift axial gravity high: a re-interpretation. Tectonophysics, 204(1-2): 59-70.

Teague, A., Seward, T. and Harrison, D., 2008. Mantle source for Oldoinyo Lengai carbonatites: Evidence from helium isotopes in fumarole gases. Journal of Volcanology and Geothermal Research, 175(3): 386-390.

Tu, K.P., Brooks, P.D. and Dawson, T.E., 2001. Using septum-capped vials with continuous-flow isotope ratio mass spectrometric analysis of atmospheric CO_2 for Keeling plot applications. Rapid Communications in Mass Spectrometry, 15(12): 952-956.

Vauchez, A., Dineur, F. and Rudnick, R., 2005. Microstructure, texture and seismic anisotropy of the lithospheric mantle above a mantle plume: insights from the Labait volcano xenoliths (Tanzania). Earth and Planetary Science Letters, 232(3-4): 295-314.

Viveiros F., Cardellini C., Ferreira T., Caliro S., Chiodini G., Silva C., 2010, Soil CO_2 emissions at Furnas volcano, São Miguel Island, Azores archipelago: Volcano monitoring perspectives, geomorphologic studies, and land use planning application: Journal of Geophysical Research, v. 115, B12208,

Viveiros, F., T. Ferreira, J. Cabral Vieira, C. Silva, and J. L. Gaspar. 2008. Environmental influences on soil CO 2 degassing at Furnas and Fogo volcanoes (São Miguel Island, Azores archipelago). *Journal of Volcanology and Geothermal Research* 177, 883-893.

Vye-Brown, C., Smith, K. and Wright, T., 2013. Active rifting, magmatism and volcanism in the Afar Depression, Ethiopia. Large Igneous Provinces Commission.

Wamalwa, A.M. and Serpa, L.F., 2013. The investigation of the geothermal potential at the Silali volcano, northern Kenya Rift, using electromagnetic data. Geothermics, 47: 89-96.

Werner, C. and Brantley, S., 2003. CO_2 emissions from the Yellowstone volcanic system. Geochemistry, Geophysics, Geosystems, 4(7): 1061.

Werner, C., Brantley, S.L. and Boomer, K., 2000. CO_2 emissions related to the Yellowstone volcanic system: 2. Statistical sampling, total degassing, and transport mechanisms. Journal of Geophysical Research, 105(B5): 10831-10846.

Werner, C., Evans, W.C., Kelly, P.J., McGimsey, R., Pfeffer, M., Doukas, M. and Neal, C., 2012. Deep magmatic degassing versus scrubbing: Elevated CO_2 emissions and C/S in the lead-up to the 2009 eruption of Redoubt Volcano, Alaska. Geochemistry, Geophysics, Geosystems, 13(3): Q03015.

Wicks, C., Thatcher, W. and Dzurisin, D., 1998. Migration of fluids beneath Yellowstone caldera inferred from satellite radar interferometry. Science, 282(5388): 458-462.
Wright, T., Ebinger, C., Biggs, J., Ayele, A., Yirgu, G., Keir, D. and Stork, A., 2006. Magma-maintained rift segmentation at continental rupture in the 2005 Afar dyking episode. Nature, 442(7100): 291-294.

Table 1: Mean flux, proportion and error bounds for the two diffuse CO_2 flux populations measured at Longonot volcano in late-2012.

Flux Population	Mean flux ($gm^{-2}d^{-1}$)	95% confidence limit ($gm^{-2}d^{-1}$)	Proportion (%)
A	30	6.8-76	5
B	0.9	0.3-2.3	95

Table 2: Estimates of total emissions at the three major degassing sites at Longonot volcano. The total CO_2 output is calculated using the mean flux of Population A, 30 g m^2 d^1. * The value in brackets uses the 95th percentile values of Population A (6.8 – 76 g m^2 d^1) to gain upper and lower limits of the total CO_2 output.

Locality	Total area degassing (m^2)	Total CO_2 output (kg d^{-1})
Crater wall	7-8,000	0.2-240
Crater floor	7-100	0.2-3
Pyroclastic cones	10-500	0.3-15
Total	24-8,6000	0.7-258 (0.16-650)*

Table 3: Composition of fumarolic gas samples from Longonot volcano. $\delta^{13}C$ (‰) = $[(^{13}C/^{12}C)_{sample}/(^{13}C/^{12}C)_{standard} -1]$ x 1, 000; the standard for C isotopes is PeeDee Belemnite (PDB). N/D = not detected.

Sample	Easting	Northing	H_2 (ppm)	He (ppm)	CH_4 (ppm)	N_2 (%)	O_2 (%)	Ar (%)	CO_2 (%)	$\delta^{13}C$ (‰)	CO_2 flux g $m^{-2}d^{-1}$
ER15.1	216631	9899568	1.81	14.9	1.8	77.02	21.98	0.794	0.21		14.5
ER15.2	216631	9899568	1.11	13.2	3.8	76.81	22.14	0.797	0.25	-6.36	

ER16.1	216616	9899564	1.59	12.0	N/D	76.97	21.86	0.817	0.36		76.15
ER16.2	216616	9899564	1.55	19.7	N/D	77.24	21.60	0.809	0.35	-4.75	
ER17.1	216590	9900240	1.37	11.0	N/D	77.19	21.79	0.822	0.19		16.6
ER18.1	216642	9900254	1.23	15.7	N/D	77.33	21.65	0.808	0.22	-5.00	51.8
Precision			2%	1%	2%	0.1%	0.1%	0.1%	2%		

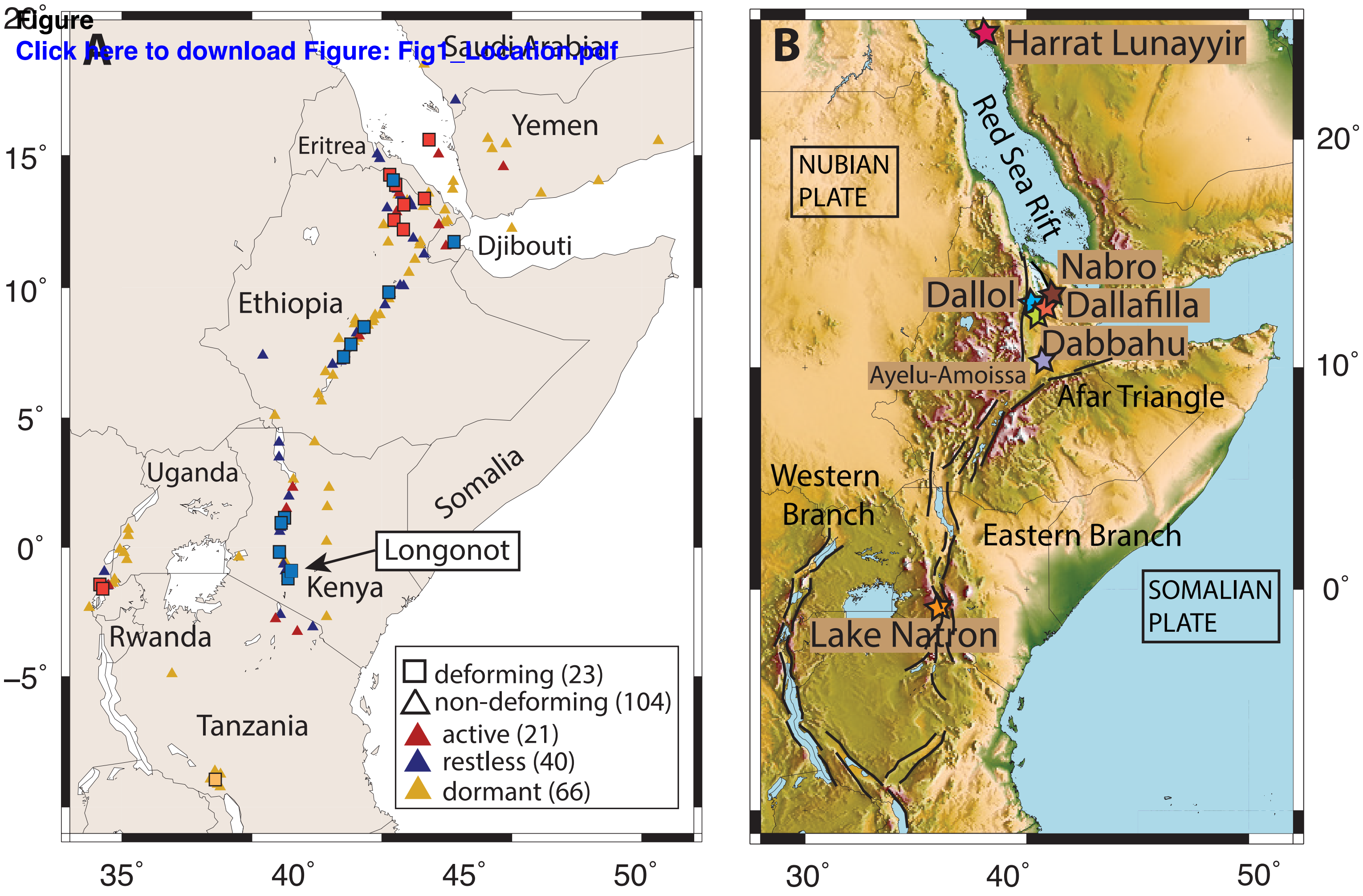
A
Saudi Arabia
Yemen
Eritrea
Djibouti
Ethiopia
Somalia
Uganda
Longonot
Kenya
Rwanda
Tanzania
deforming (23)
non-deforming (104)
active (21)
restless (40)
dormant (66)
20˚
15˚
10˚
5˚
0˚
–5˚
35˚
40˚
45˚
50˚
B
Harrat Lunayyir
Red Sea Rift
NUBIAN
PLATE
Nabro
Dallol
Dallafilla
Dabbahu
Ayelu-Amoissa
Afar Triangle
Western
Branch
Eastern Branch
SOMALIAN
PLATE
Lake Natron
20˚
10˚
0˚
30˚
40˚
50˚

Figure

Click here to download Figure: Fig2_GeologicalMap.pdf

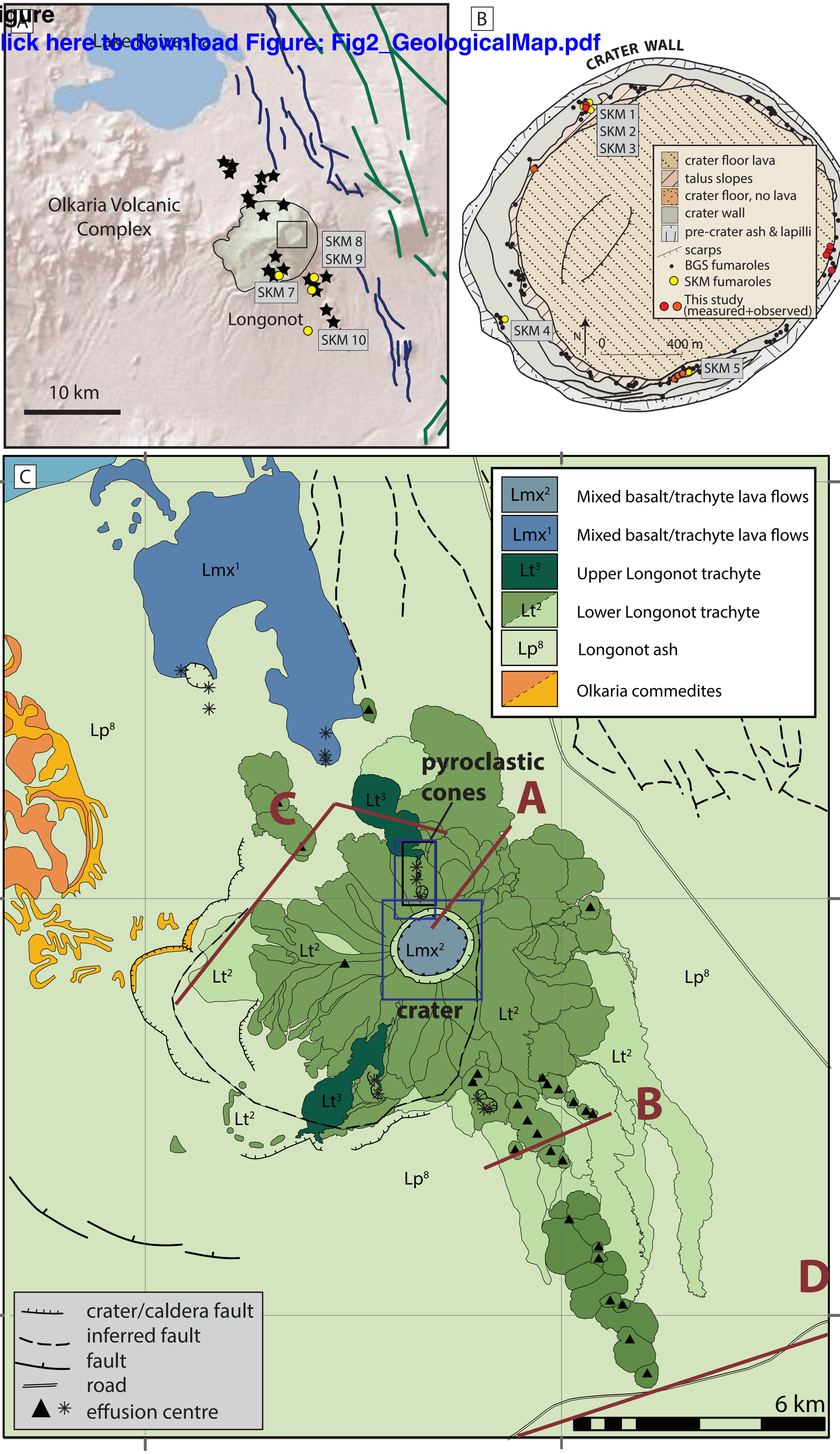

Figure
Click here to download high resolution image

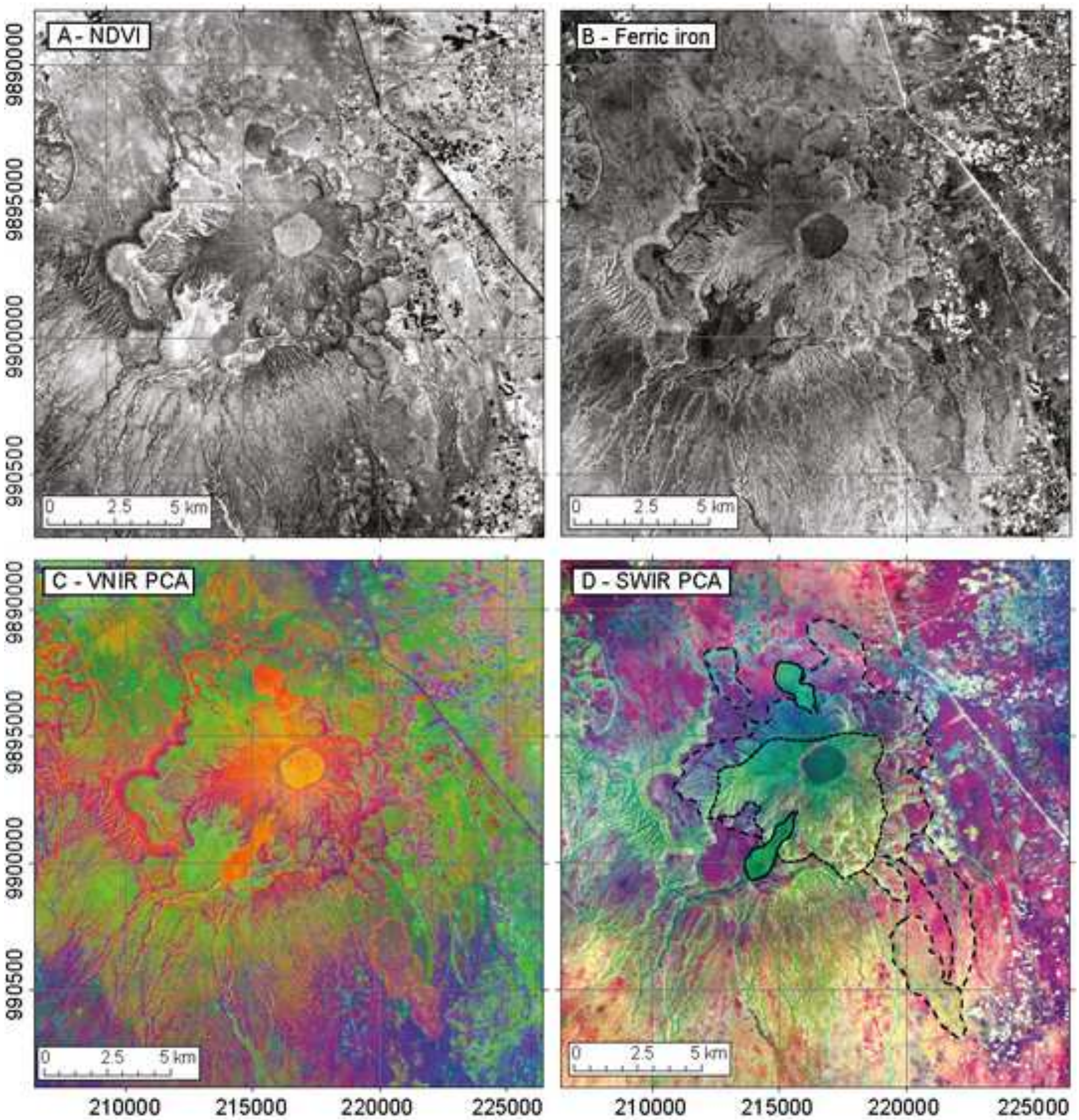

Figure 2
Click here to download Figure: Fig4_Geochemistry.pdf

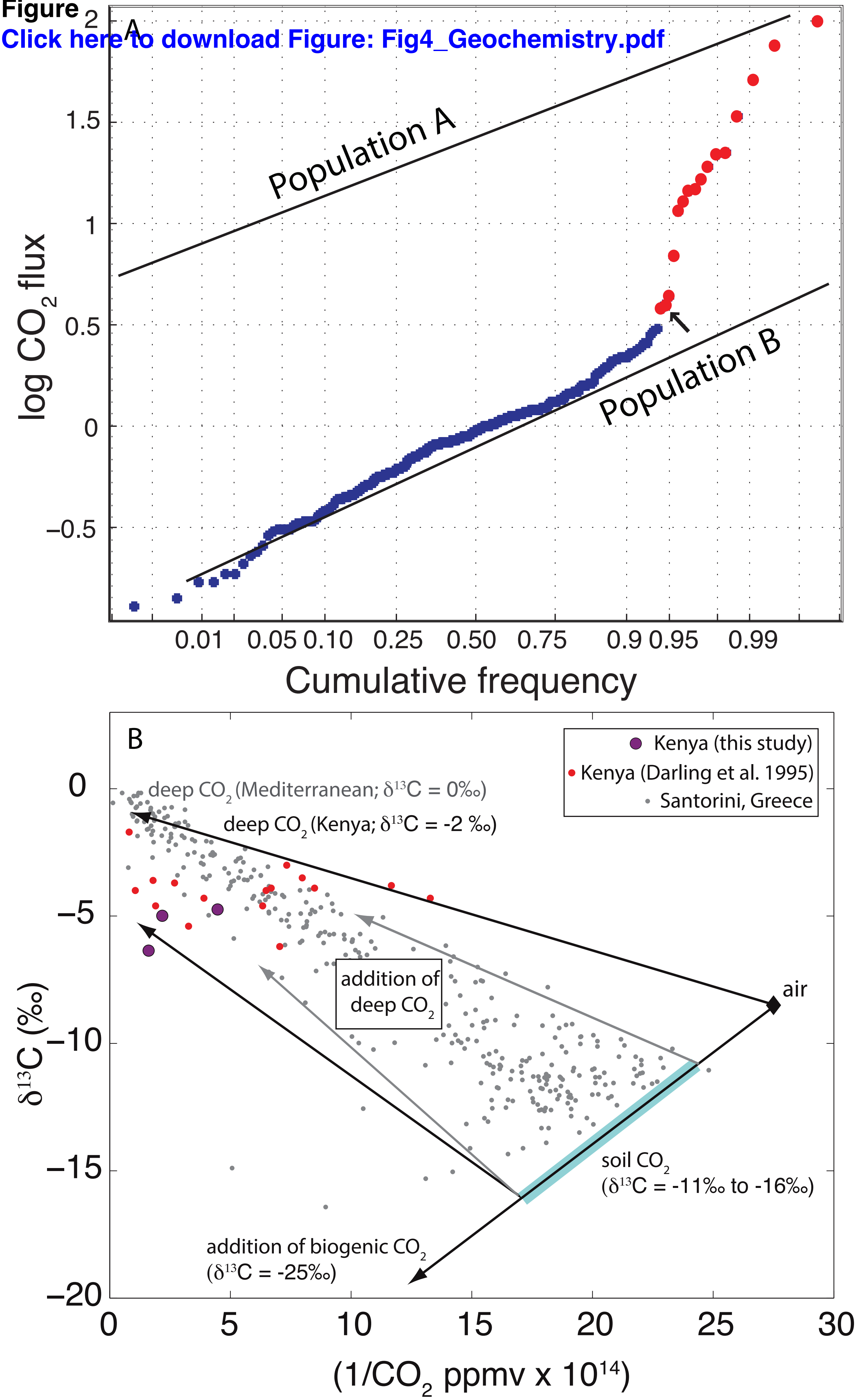


A) Crater wall fumarole
B) Crater floor fumarole
C) Pyroclastic cone fossil fumarole
D) Geothermal grass

Figure

[Click here to download high resolution image]

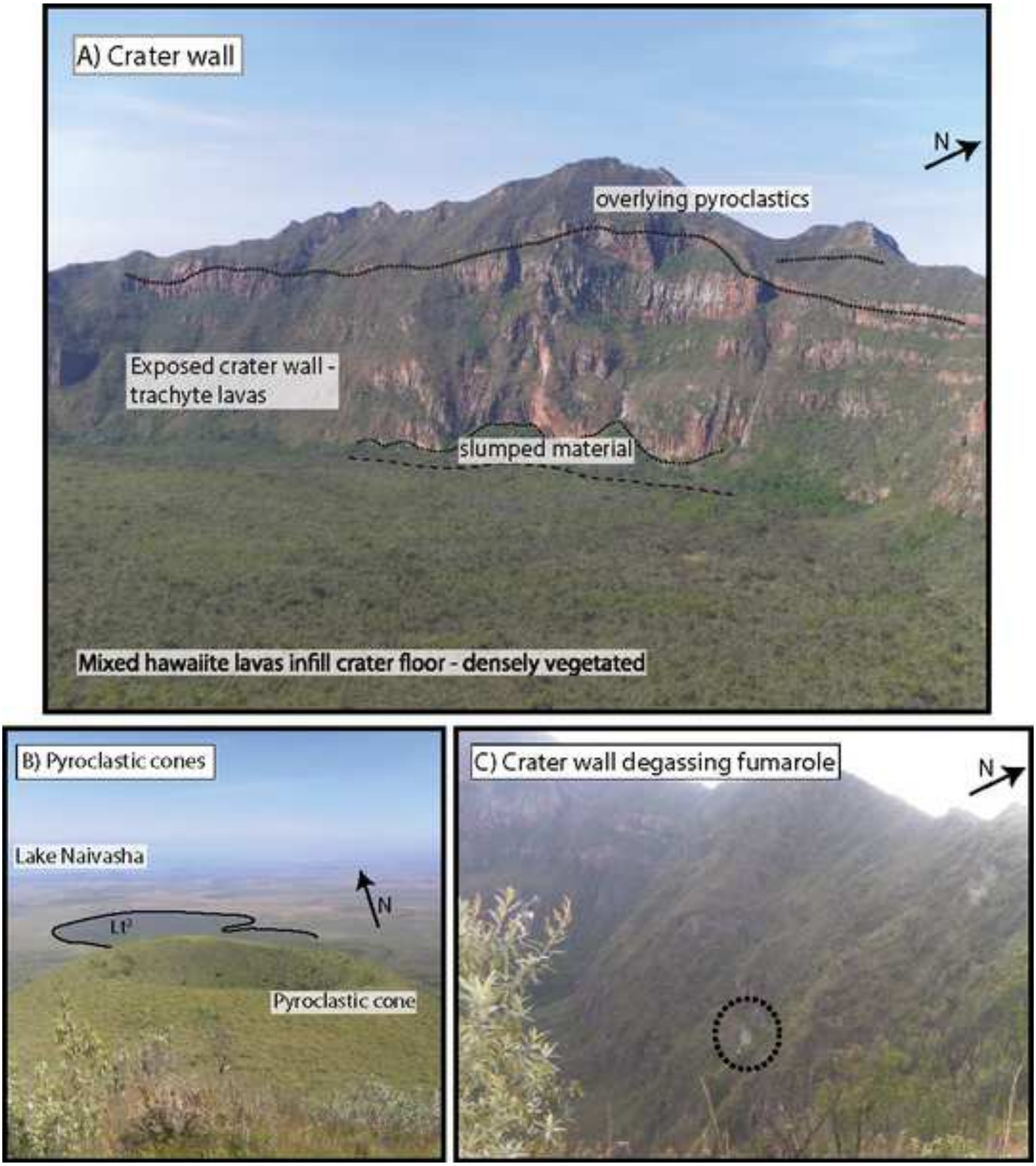

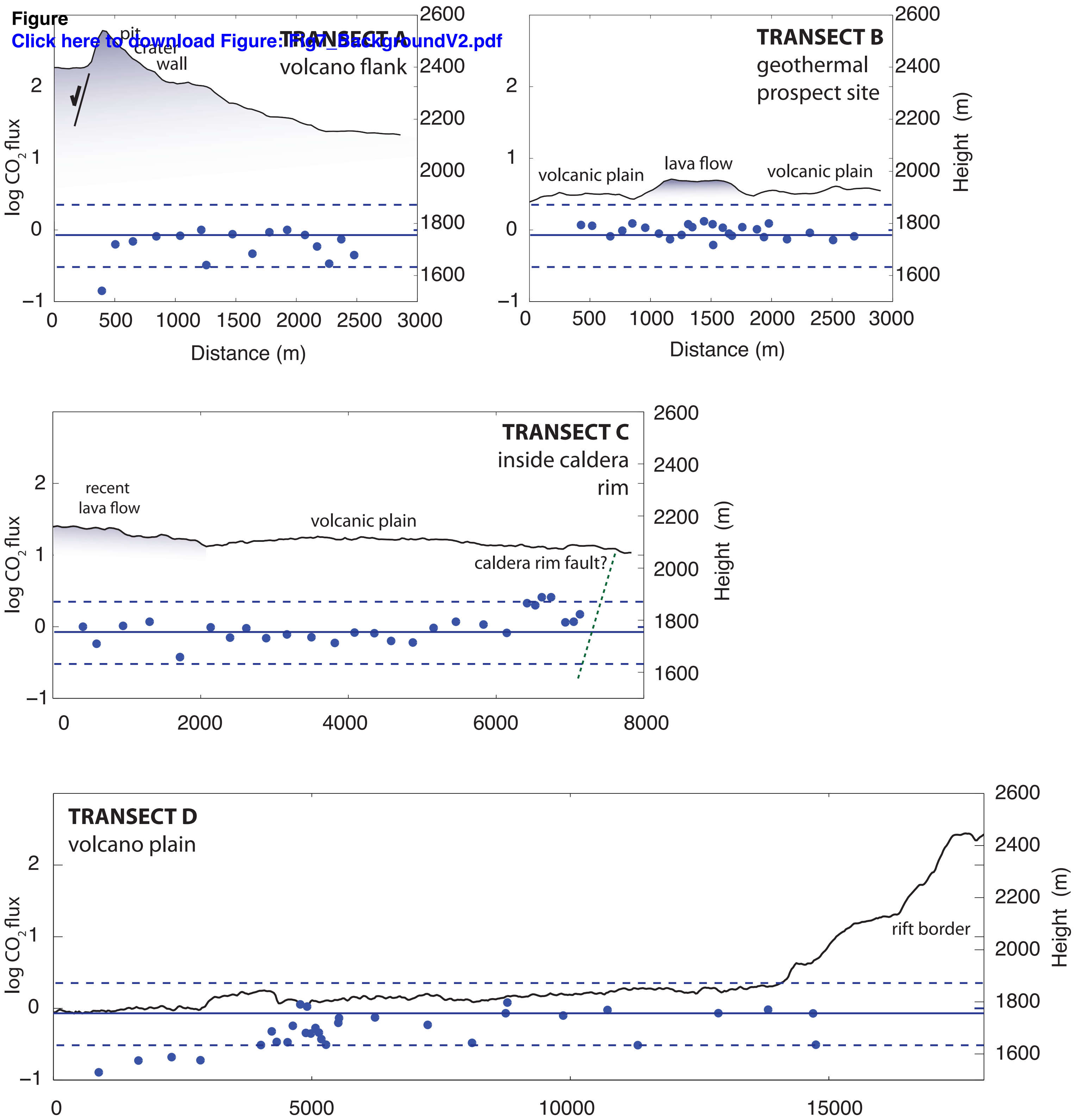
TRANSECT A
volcano flank
pit
crater
wall
log CO2 flux
Distance (m)
TRANSECT B
geothermal
prospect site
volcanic plain
lava flow
volcanic plain
Distance (m)
Height (m)
TRANSECT C
inside caldera
rim
recent
lava flow
volcanic plain
caldera rim fault?
log CO2 flux
Height (m)
TRANSECT D
volcano plain
rift border
log CO2 flux
Height (m)

Figure

Click here to download Figure: Fig8_craterwall.pdf

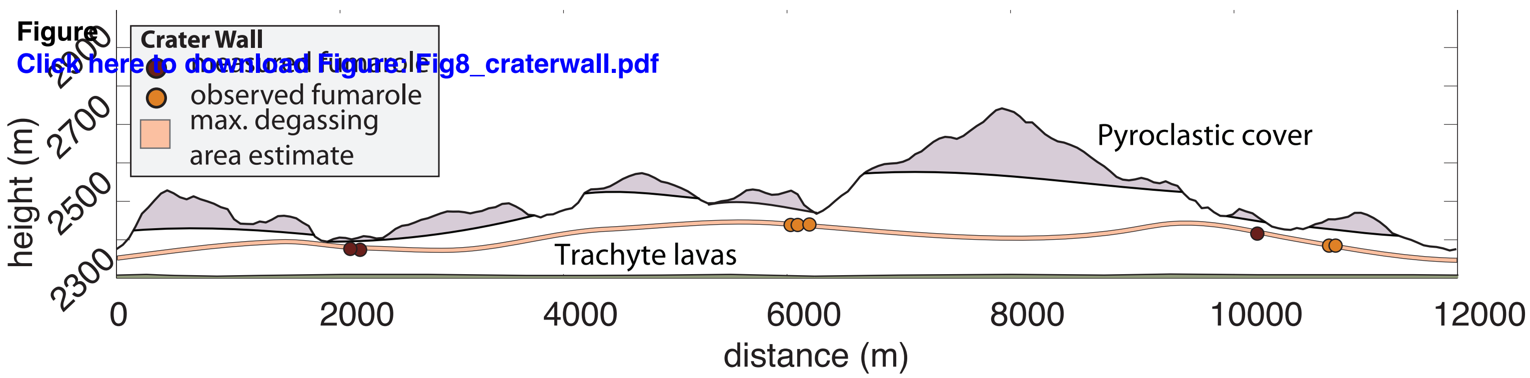

Figure
Click here to download Figure: Fig9_Degassing.pdf

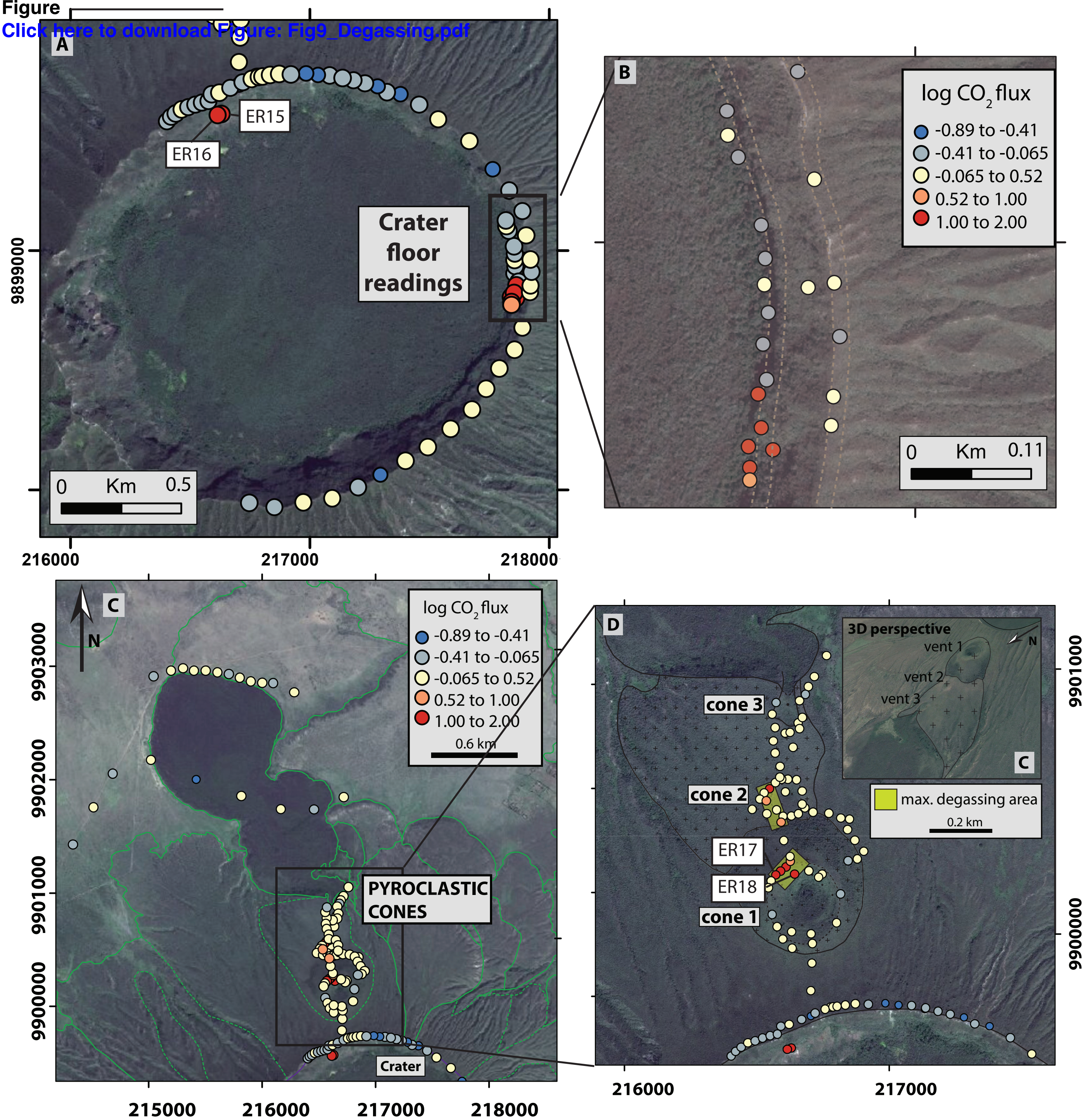

Electronic Supplementary Material (online publication only)
Click here to download Electronic Supplementary Material (online publication only): supp.xlsx